Benefits of a 4th Ice Class in the Simulated Radar Reflectivities of Convective Systems using a Bulk Microphysics Scheme

Stephen E. Lang[1,2], Wei-Kuo Tao[1], Jiun-Dar Chern[1,3], Di Wu[1,2], and Xiaowen Li[1,3]

[1]*Mesoscale Atmospheric Processes Laboratory*
NASA Goddard Space Flight Center
Greenbelt, MD

[2]*Science Systems and Applications, Inc.*
Lanham, MD77

[3]*Morgan State University*
Baltimore, MD

Journal of the Atmospheric Sciences

Submitted October 18, 2013

Revised February 18, 2014

2nd Revision May 22, 2014

Corresponding author address: Stephen Lang, Mesoscale Atmospheric Processes Laboratory, Code 612, NASA GSFC, Greenbelt, MD 20771

Email: Stephen.E.Lang@nasa.gov

ABSTRACT

Current cloud microphysical schemes used in cloud and mesoscale models range from simple one-moment to multi-moment, multi-class to explicit bin schemes. This study details the benefits of adding a 4th ice class (frozen drops/hail) to an already improved single-moment 3-class ice (cloud ice, snow, graupel) bulk microphysics scheme developed for the Goddard Cumulus Ensemble model. Besides the addition and modification of several hail processes from a bulk 3-class hail scheme, further modifications were made to the 3-ice processes, including allowing greater ice supersaturation and mitigating spurious evaporation/sublimation in the saturation adjustment scheme, allowing graupel/hail to transition to snow via vapor growth and hail to transition to graupel via riming, wet graupel to become hail and the inclusion of a rain evaporation correction and vapor diffusivity factor. The improved 3-ice snow/graupel size-mapping schemes were adjusted to be more stable at higher mixing rations and to increase the aggregation effect for snow. A snow density mapping was also added.

The new scheme was applied to an intense continental squall line and a moderate, loosely-organized continental case using three different hail intercepts. Peak simulated reflectivities agree well with radar for both the intense and moderate case and were superior to earlier 3-ice versions when using a moderate and large intercept for hail, respectively. Simulated reflectivity distributions versus height were also improved versus radar in both cases compared to earlier 3-ice versions. The bin-based rain evaporation correction affected the squall line more but overall agreement in reflectivity distributions was unchanged. The new scheme also improved the simulated surface rain rate histograms.

1. Introduction

Atmospheric cloud modeling has benefited immensely from the continued improvement in computational power. Simulations using explicit spectral bin microphysics (SBM) with large 3D domains in mesoscale models like WRF (the Weather Research and Forecasting model, Michalakes et al. 2004; Skamarock et al. 2008) can now be performed (Iguchi et al. 2012a, b). In addition to higher resolution (e.g., Khairoutdinov and Randall 2006) and the advent of MMFs (multi-scale modeling frameworks, Randall et al. 2003, Tao et al. 2009), cloud-resolving simulations have also benefited in the form of ever more sophisticated microphysics. Simple bulk liquid (e.g., Kessler 1969) and ice schemes (e.g., Wisner et al. 1972) with only a few categories have grown into multiple ice categories (e.g., Straka and Mansell 2005), two moments (e.g., Ferrier 1994; Reisner et al. 1998; Morrison et al. 2009) and higher (Milbrandt and Yau 2005b), and highly detailed SBM (Ovtchinnikov and Kogan 2000; Khain et al. 1999; 2000; 2004). Detailed bin forms originated a while ago but are only now becoming practical, having previously been limited to either 1D (Young 1974; Scott and Hobbs 1977), 2D (Takahashi 1976; Hall 1980; Reisin et al. 1996; Khain and Sednev 1996) or without ice (Kogan 1991).

Though the ability to use SBM with ever increasing 3D domains is becoming a reality, these types of simulations are still not common, and there is a trade-off versus bulk microphysics schemes (BMSs), which assume hydrometeor distributions follow a prescribed form (typically exponential or gamma). BMSs are much faster and require a lot less memory. For certain applications (e.g., very large domains or long-term simulations), computational resources are often not sufficient for SBM, which themselves are still not perfect (Li et al. 2010); these resources could also be applied to better resolution, which is another important consideration when it comes to realistically simulating convective entrainment and overturning (Bryan et al.

95 2003). BMSs are typically invoked using either one-moment (1M, only mass is predicted) or
96 two-moments (2M, both mass and number concentration are predicted); these schemes have also
97 seen numerous advancements and improvements in recent years. Numerous modeling studies
98 and BMSs were made or based on the 1M 3-class ice (3ICE) schemes of Lin et al. (1983) and
99 Rutledge and Hobbs (1983, 1984) developed in the early 1980's. These schemes were the
100 workhorses of cloud microphysics for many years and are still used in some form by many
101 schemes today, especially for NWP. However, they do have their biases (Lang et al. 2007, 2011;
102 hereafter L2007, L2011) and are susceptible to thresholding phenomena (Rutledge and Hobbs
103 1984). They use *a priori* hydrometeor classes of cloud ice, snow and either graupel or hail and
104 transfer hydrometeors from one class to another conditional upon specified thresholds; this can
105 result in abrupt and unnatural behavior and diverging solutions depending on if conditions are
106 met. An innovative approach was recently developed by Morrison and Grabowski (2008) based
107 on the concepts of Heymsfield (1982) and Hashino and Tripoli (2007) whereby the amounts of
108 mass acquired by riming and deposition are predicted separately. This allows for the history of
109 the riming fraction to be accounted for and results in a spectrum of particle densities with
110 smooth, natural transitions from ice to snow and snow to graupel. Lin and Colle (2011) included
111 the effects of partially rimed particles using a diagnostic riming intensity as well as functional
112 forms of the mass-, area- and velocity-diameter relationships. In general, the representation of
113 cloud microphysical processes is constantly improving as more and more schemes are including
114 aerosols and the representation of ice processes continues to improve (Muhlbauer et al. 2013).
115 Two-moment BMSs have become increasingly popular (Ziegler et al. 1985; Ferrier 1994;
116 Reisner et al. 1998; Meyers et al. 1997; Milbrandt and Yau 2005a; Morrison et al. 2005, 2009;
117 Seifert and Beheng 2006; Thompson et al. 2008; Lim and Hong 2010) and offer a good

compromise between the extreme cost of SBM and the restriction of 1M BMSs. They allow an extra degree of freedom in defining the hydrometeor distributions compared to 1M schemes and can account for size-sorting (Milbrandt and Yau 2005a) and aggregation as well as aerosol effects (Lim and Hong 2010). Two-moment schemes are also superior to 1M in terms of rain evaporation. A fixed rain intercept in 1M schemes tends to produce excessive rain evaporation, namely in the stratiform region; this can be alleviated with 2Ms, which can lead to better convective and stratiform rainfall structures (Morrison et al. 2009).

However, 2M schemes as well as SBM require observed cloud condensation nuclei (CCN) and/or ice nuclei (IN) profiles to activate cloud water and/or ice particles, and despite their potential (Ferrier et al. 1995; Milbrandt and Yau 2005a; Morrison et al. 2009), there are enough uncertainties and nonlinearities that more advanced/sophisticated schemes do not always perform better than simpler 1M bulk schemes (Wang et al. 2009; Varble et al. 2011). Besides the extra degrees of freedom that are required to behave in a realistic manner, larger errors in a more dominant process can overwhelm potential gains elsewhere. WRF contains a variety of microphysics packages, including 1M, 2M and schemes that are a mixture of both, easily allowing comparisons between the various schemes. Van Weverberg et al. (2013) used the Advanced Research WRF to evaluate MCS simulations using three different BMSs over the tropical western Pacific and found that although different, the results from the 2M schemes were not superior to those using 1M; they found the most crucial element was the fall speeds of frozen particles. Using WRF, Han et al. (2013) found that the 2M Thompson scheme (Thompson et al. 2008) had the best radar reflectivities for a winter storm but the fall velocities from the Goddard scheme (Tao and Simpson 1993; Tao et al. 2003; L2007) agreed best with vertical profiler observations. Powell et al. (2012) used vertically-pointing millimeter radar observations to

141 evaluate WRF simulations of MCS anvils near Niamey, Niger; they found the 1M Goddard and
142 WDM6 (Lim and Hong 2010, which has 1M ice and 2M liquid) schemes actually produced more
143 realistic anvils than did the 2M ice schemes. Systematic biases in cloud-resolving model (CRM)
144 BMSs were first identified when CRM simulations were used for satellite retrievals. Radiative
145 transfer models applied to CRM-simulated cloud fields revealed distributions that contained
146 excessive scattering signatures that were not representative of actual observed distributions
147 (Panegrossi et al. 1998; Bauer 2001; Olson et al. 2006). In addition to the excessive scattering,
148 several studies found excessively high reflectivities in the upper troposphere of CRM simulations
149 with excessive amounts and/or sizes of precipitation-sized ice produced by the BMSs as the
150 primary reason (L2007, L2011; Blossey et al. 2007; Zhou et al. 2007; Li et al. 2008; Matsui et al.
151 2009). Typically, the problem is associated with graupel (L2007; Li et al. 2008; Matsui et al.
152 2009). Though somewhat confirmed by Varble et al. (2011), they noted that excessively high
153 reflectivities can also be due to snow in a 2M scheme (Morrison et al. 2009) and that reasonable
154 reflectivities can be obtained using nonspherical graupel particles with variable density and
155 mass-diameter relationships with 1M. At any rate, there are enough inherent biases and room for
156 improvement that microphysics schemes in general require and continue to undergo refinement.
157 This study is a follow on to L2007 and L2011 and details the continued improvement and
158 enhancement of the Goddard 1M BMS used in the Goddard Cumulus Ensemble model (GCE), a
159 version of which (L2007) is one of the microphysics packages available in WRF. This scheme
160 has been evaluated in WRF and despite some continued biases (L2007, L2011) found to compare
161 quite well relative to other WRF schemes with regard to snow fallspeeds (Han et al. 2013) and
162 MCS anvils. The lineage is built upon the Rutledge and Hobbs (1983, 1984) 3ICE-graupel
163 version. Despite the improvements already made to the scheme (L2007, L2011), it still contains

some unrealistic aspects with regard to reflectivity structure and, without hail, lacks the ability to simulate more intense radar echoes. Hail allows for the simulation of much more intense radar echoes and much higher fall velocities than graupel and can thus to first order expand the scheme to cover a far wider range of conditions than would be possible with say improving the graupel category to 2M. This study details the addition of a 4th ice category, which encompasses the spectrum of particles from smaller frozen drops to larger hail stones that have a high density (~0.9 g cm^{-3}) as a result of being or having a coating at or near liquid at some point in their history, as well as further refinements to the scheme that result in an improved 4-class ice (4ICE) version of the Goddard 1M BMS. Despite the benefits of a smooth transition in particle characteristics (e.g., density) with a single prognostic rimed-ice category, higher and lower-density particles cannot coexist in such a scheme without a separate hail category, which may be necessary to simulate for example a narrow hail shaft (Milbrandt and Morrison 2013). The new Goddard 4ICE scheme is tested for two cases, an intense midlatitude squall line observed during MC3E and a more moderate convective case from TRMM LBA (the Tropical Rainfall Measuring Mission Large-Scale Biosphere-Atmosphere Experiment in Amazonia). The model results are evaluated using radar reflectivity contoured frequency with altitude diagrams (CFADs, Yuter and Houze 1995). Validation via comparison with *in situ* aircraft data can provide a very detailed look at the performance of microphysical schemes (e.g., Molthan and Colle 2012); however, such data are limited and difficult to compare against (if even available) when it comes to convective cores and are essentially unavailable when it comes to intense convective cores. Another approach has been to compare modeled versus observed radiances, often radar reflectivity, statistically in the form of CFADs, the primary approach adopted in L2007 and L2011. CFADs, which are essentially PDFs sampled at discrete levels through the

187 depth of a storm stacked in the vertical and then contoured, were first used primarily to
188 characterize observations (e.g., Yuter and Houze 1995). Lin (1999) and Lang et al. (2003)
189 constructed CFADs of model data, but Smedsmo et al. (2005), Eitzen and Xu (2005) and Braun
190 (2006) were the first to use radar CFADs to actually evaluate CRM performance. These were
191 quickly followed by several other studies (Blossey et al. 2007; L2007; Rogers et al. 2007; Zhou
192 et al. 2007; Li et al. 2008), establishing this method (or a close variation thereof) as a standard
193 way of evaluating CRM-type simulations (L2011; Varble et al. 2011; Iguchi et al. 2012a; Powell
194 et al. 2012; Guy et al. 2013; Han et al. 2013; Van Weverberg et al. 2013; Wu et al. 2013).
195 Though there are other ways to evaluate the performance of CRMs and their microphysics
196 schemes, having to match the observed radar reflectivity distributions is a more stringent test
197 than mean quantities (Powell et al. 2012). Radar observations are more readily available than *in*
198 *situ* observations, especially when it comes to convection, and the resolution of the data is
199 comparable to CRM grids and much better than satellite observations.
200 The main objectives of this study are to allow the improved 1M Goddard BMS (L2007; L2011)
201 to simulate intense convection via the addition of hail and to further improve upon the model's
202 overall performance via the reduction of biases in the synthetic radar structure and reflectivity
203 distributions. The paper is organized as follows. Section 2 describes the Goddard CRM, the
204 changes to the Goddard microphysics, the two case studies, and the numerical experiments.
205 Section 3 presents the simulation results and their validation using radar observations as well as
206 surface rain intensities. The summary and conclusions are given in section 4.
207
208 **2. Simulation setup and cases**
209

a. The Goddard Cumulus Ensemble model (GCE)

The new Goddard 1M 4ICE BMS is evaluated using the 3D GCE. The GCE was described in Tao and Simpson (1993) and Tao *et al.* (2003) and more recently in Tao *et al.* (2013). The model configuration closely follows that used in L2011. The GCE has a one-and-a-half order sub-grid scale turbulence scheme (Soong and Ogura 1980), parameterizations for shortwave (Chou and Suarez 1999), longwave (Chou and Kouvaris 1991; Chou et al. 1995, 1999; Kratz et al. 1998) and cloud optical properties (Sui et al. 1998; Fu and Liou 1993), positive definite advection (Smolarkiewicz 1983, 1984; Smolarkiewicz and Grabowski 1990), and options for anelastic (Ogura and Phillips 1962) or compressible flow (Klemp and Wilhelmson 1978). The GCE has several microphysics options, but the primary BMS is the Rutledge and Hobbs (1983, 1984)-based 3ICE-graupel scheme (i.e., cloud water, rainwater, cloud ice, snow and graupel), which has been improved to reduce unrealistically large amounts of graupel (L2007) and 40 dBZ echoes above the freezing level (L2011) and modified to introduce ice nuclei concentrations into the Bergeron parameterization (Zeng *et al.* 2008, 2009).

b. Addition of hail processes and other microphysics improvements

Prior improvements reduced excessive amounts of graupel (L2007) and excessive penetrations of 40-dBZ echoes above the freezing level (L2011), alleviating some of the biases in the original Goddard 1M 3ICE-graupel scheme. The improved versions, however, have two artifacts in their simulated reflectivity structure. Time-height cross sections of peak reflectivities show a band of elevated reflectivity maxima above the freezing level separated by corresponding local minima

233 just above the freezing level (e.g., Figs. 2c-d, 6d) as opposed to observations, which typically
234 show a steady monotonic decrease with height (e.g., Figs. 2a, 6a). The snow/graupel size
235 mapping implemented in L2011 tried to compensate for this and still produce reasonable peak
236 reflectivities by rapidly increasing the particle sizes (especially snow) at moderate to high mixing
237 ratios (Figs. 1c-d). This can lead to spurious artifacts in the reflectivity distributions near the
238 melting layer for stronger cases (Fig. 4d). To address these issues and allow the scheme the
239 ability to simulate more intense convection, a 4th ice class (frozen drops/hail) was added and the
240 scheme further refined to produce an improved Goddard 4ICE scheme.
241 Table 1 lists the changes in relation to previous versions of the scheme, which are detailed
242 below. Hail processes based on Lin et al. (1983) were added with some modification. Hail
243 riming, accretion of rain, deposition/sublimation, melting, shedding and wet growth processes
244 were left unchanged. Analogous to L2007 for graupel, the collection of other ice particles under
245 dry growth conditions (dry collection) was eliminated for hail to prevent an excessive buildup of
246 hail as collection efficiencies should be minimal; but, hail near wet growth conditions is
247 expected to be close to water coated and thus efficiently collect other ice particles. Hail within
248 95% of wet growth is thus allowed to collect other ice particles. Graupel is medium density
249 (~0.3 to 0.5 g cm^{-3}) and mainly a riming product; frozen drops, however, are high-density (~0.9 g
250 cm^{-3}) like that of solid ice or hail. Therefore, the new scheme differentiates hail initiation from
251 graupel by treating the product of any process that freezes rain as hail. Five new hail processes
252 were also added: wet hail accretion of graupel, hail rime splintering, wet graupel conversion to
253 hail, hail conversion to snow due to depositional growth (also added for graupel) to allow
254 hail/graupel particles that undergo significant deposition at cold temperatures in the absence of
255 liquid water to transition to snow, and hail conversion to graupel via riming, which tries to

account for lower hail bulk densities due to rime accumulation under non wet growth conditions. Milbrandt and Morrison (2013) demonstrated how graupel densities can sharply decrease at colder temperatures aloft when accounting for variable rime density. A similar analogy is applied here with regard to the hail category, which too can be rimed. The latter two processes are "apparent" and try to overcome some of the limitations associated with having fixed particle categories by providing additional pathways for particles to change from one category to another.

In addition to the hail processes, further modifications were made to the improved 3ICE processes. Snow autoconversion was strengthened by adjusting the timescale, threshold and efficiency in the Kessler-type formulation. The original formulation is quite weak, but aircraft observations of small ice particle distributions suggest that although diffusion dominates at colder temperatures, there is evidence of aggregation (Field 1999). Though autoconversion was strengthened, diffusion still remains the dominant process. The maximum snow collection of cloud ice efficiency was increased to reflect the fact that ice particles with diameters greater than about 200 microns are efficient collectors. A water vapor diffusivity correction factor (Byers 1965) was applied to all related processes, effectively replacing a more simplified function of pressure and temperature. The formulation for the depositional growth of cloud ice into snow (i.e., Psfi) invokes the time step over a time scale, so that tiny amounts of snow can form even when cloud ice is quite small (i.e., the time scale to become snow is large). Therefore, an arbitrary small threshold was introduced before activating this term[1]. With ice supersaturations commonly observed on the order of tens of percent (Jensen et al. 2001; Stith et al. 2002; Garrett et al. 2005), the sequential saturation adjustment scheme (Tao et al. 2003) was further relaxed from the 10% constraint in L2011 to a maximum of 20%. The deleterious effects of cloud

[1] A value of 1.e-5 g/g scaled by the surface air density over the level air density was used to inhibit this artificial snow production mainly because it has a noticeable effect on longer-term (i.e., MMF) simulations.

boundaries advecting through an Eulerian grid (e.g., spurious evaporation) have been previously noted [Klaassen and Clark 1985; Grabowski 1989; Grabowski and Smolarkiewicz 1990; Stevens et al. 1996; Grabowski and Morrison 2008; Reisner (personal communication)]. To reduce these effects, the saturation adjustment was further modified to restrict cloud evaporation and sublimation to subsidence areas. The time-scale for ice sublimation can be appreciable, allowing even smaller ice particles to exist in subsaturated conditions (e.g., Garrett et al. 2005); so, the saturation adjustment was relaxed to allow cloud ice to persist under ice subsaturated conditions.

With the addition of hail, the size-mapping scheme for snow and graupel introduced in L2011 was adjusted. The rate at which the characteristic size (i.e., inverse of the slope parameter) increases with mixing ratio, especially of snow, was lowered (see Fig. 1). As will be shown, peak reflectivities are now determined largely by hail and do not require large graupel or snow particles to generate these higher values. In addition, the aggregation effect, especially for snow, was increased to allow particle sizes to grow more rapidly as temperatures rise from -25 C, and an associated snow density mapping (Fig. 1g) was introduced as a function of snow size (i.e., Brandes et al. 2007). Graupel density was also divided into low and moderate based on a simple mixing ratio threshold. Finally, to address the problem of excessive rain evaporation due to a fixed rain intercept, a rain evaporation correction was adopted based on the results from an explicit bin microphysics scheme (Li et al. 2009). This correction was made "physical" by lowering the rain intercept (i.e., increasing the mean raindrop diameter) locally for each rain grid cell until the new evaporation rate matched the correction factor. The scaling was capped such that rain size never increases with decreasing rain mixing ratio.

For a more detailed description of the new scheme, including the new hail budget equation, rain evaporation correction and snow mapping, please see the Appendix.

c. Convective case studies

1) AN INTENSE MIDLATITUDE SQUALL LINE: MC3E

The Midlatitude Continental Convective Clouds Experiment (MC3E) was conducted in and around central Oklahoma (OK) from April to May 2011 as a collaborative effort between the DOE (Department of Energy) ARM (Atmospheric Radiation Measurement) and NASA GPM (Global Precipitation Measurement) programs. The 20 May 2011 case featured a deep, upper-level low over the central Great Basin moving into the central and southern Rockies before lifting into the central and northern Plains. At the surface, low pressure in southeastern Colorado drew warm, moist air up through the southern Plains to a warm front oriented E-W across Kansas, while a dry line extended from the Texas/Oklahoma Panhandle down through the Concho Valley. The result was a series of convective lines that formed over the Great Plains and propagated eastward toward the Mississippi Valley. The most intense squall line to pass through the MC3E sounding network was the result of convection that had developed over south-central Kansas (KS) and north-central OK within the network merging with the northern end of a long convective line that had formed along the dry line and extended from southwestern OK down to the Big Bend. The northern portion of this longer line entered the MC3E sounding network around 07 UTC 20 May and by 09 UTC had consolidated with the convection near the KS-OK border to form a more intense convective segment with a well-defined trailing stratiform region that then propagated through the network between 09 and 12 UTC. By 13 UTC, the convective leading edge had exited the network, leaving the network dominated by a large area of stratiform

rain. Peak reflectivities within the network exceeded 60 dBZ over a depth of several km from 2 km above and to 3 km below the freezing level, a strong sign of significant hail (May and Keenan 2005; Lerach et al. 2010), while 40 and 50 dBZ echoes reached upwards of 16 and 10 km, respectively, placing this case within the top 0.005% in intensity (i.e., 1 feature in 20,000 is as strong) with regard to 40 dBZ echo penetrations based on a TRMM observed precipitation feature climatology (Zipser et al. 2006). With 45 dBZ echoes reaching more than 10 km above the freezing level, a further indication of the presence of hail (Waldvogel et al. 1979); this case is well suited to test and evaluate the new Goddard 1M 4ICE scheme with hail.

As in previous GCE modeling studies (e.g., Zeng et al. 2007, 2008; L2011), the 3D GCE was driven by large-scale forcing data obtained from a variational analysis approach (Zhang *et al*. 2001), in this case, from the MC3E sounding network. Model experiments were run for 4 days starting at 0000 UTC 17 May and ending at 0000 UTC 21 May using 1-km horizontal grid spacing and a 256 x 256 km horizontal domain (similar in size to the sounding network) with a stretched vertical grid having 76 levels and a top near 27 km. A 2-second time step was used, and surface sensible and latent heat fluxes were imposed from the variational analysis.

2) A MODERATE TROPICAL CONTINENTAL CASE: TRMM LBA

The 23 February 1999 case was previously presented in L2007 and L2011. It was characteristic of the widespread, weaker monsoon-like convection observed within the westerly wind regime (Cifelli et al. 2002; Rickenbach et al. 2002) during TRMM LBA. It falls within about the top 1% of TRMM precipitation features (i.e., 1 feature in 100 is as strong) in terms of 40 dBZ echo height intensity (Zipser et al. 2006) and provides a good contrast to the more

intense 20 May 2011 MC3E case. On this day, daytime heating triggered widespread convection that loosely organized into southeast-northwest bands. A long thin convective band developed by 2000 UTC and by 2100 UTC was already decaying. Dual-Doppler observations were collected for the northern portion of this line where 40 dBZ echoes reached to about 7 km. Please see L2007 and L2011 for more details.

The current model setup closely follows L2011 and uses the same horizontally homogenous initial conditions based on the 1200 UTC morning sounding taken at Rebio Jaru having weak low-level northwesterly flow and a 500 m mixed-layer CAPE of 934 J kg^{-1}, cyclic lateral boundary conditions and convection initiated by imposing time-varying (diurnal) surface fluxes based on surface observations collected at two different sites (ABRACOS Hill and Ji Parana). The horizontal domain was kept at 128 x 128 km as in L2011, but the horizontal grid resolution was improved to 200 m in both directions and the time step reduced to 2 seconds. The stretched vertical grid was kept at 70 levels with a top near 23 km. The north-south oriented rectangular patch of higher sensible/lower latent heat fluxes (Ji Parana) imposed in L2011 was lengthened to 18 x 80 km (solid rectangle in Fig. 8b) and replaced by higher latent/lower sensible heat fluxes (ABRACOS) if accumulated rainfall exceeded 3 mm over the patch to allow for some cloud feedback. Simulations were run for 6 hours.

d. Numerical experiments

For each case, seven numercial experiments are conducted. Three experiments are made using previous verions of the 3ICE-graupel scheme: the original (3ice0), L2007 (3ice1), and L2011 (3ice3). Four variations of the new 4ICE scheme are tested: with smaller-, medium- and larger-

sized hail with the bin rain evaporation correction (4iceb sml, 4iceb med, and 4iceb lrg, respectively) and smaller-sized hail without the evaporation correction (4ice sml). Smaller-, medium-, and large-sized hail use fixed hail distribution intercepts of 0.0200, 0.0020, and 0.0002 cm^{-4}, respectively. See Table 2 for a list of the numerical experiments performed for these cases.

3. Simulation results and validation

a. MC3E

Figure 2b shows the 4ICE control simulation (4iceb sml) compared to the observed convective line (Fig. 2a) as it passed through north-central OK. Despite the restrictive double cyclic boundary conditions, the model captures the general organization and intensity of the system with an eastward propagating north-south oriented intense convective leading edge with a trailing stratiform region off to the northwest. A vertical east-west cross section through the center of the model domain (Fig. 2c) does show an erect intense uni-cellular convective structure, but the simulated trailing stratiform region appears to be noticeably narrower.

Time-height cross sections (Fig. 3) of NEXRAD and simulated peak radar reflectivity[2] within the MC3E sounding array and model domain are shown from 00 UTC 20 to 00 UTC 21 May 2011; the observed period 06 to 12 UTC (Fig. 3a) covers the formation of the main convective line within the sounding array until the leading edge propagated out of the array. Peak reflectivities within this line exceeded 60 dBZ with 50 dBZ echoes reaching 9 km and 40 dBZ echoes 15 km. At 06 UTC, the simulations are still quite weak. The model imposed large-scale

[2] Simulated radar reflectivities were calculated from model rain, snow, graupel and hail contents assuming inverse exponential size distributions and accounting for all size mappings using the formulation of Smith et al. (1975) and Smith (1984).

392 forcing is horizontally uniform and first results in a patchwork of smaller convective cells over
393 the domain that require 2-3 hours to respond to the organizing shear and form into a squall line
394 (~09 UTC). The 3ICE graupel runs (Figs. 3b-d) significantly underestimate the peak intensity of
395 the observed squall line above the freezing level. The 3ice1 and 3ice3 runs produce a band of
396 elevated reflectivity maxima 3 km above the freezing level whereas the observed reflectivities
397 monotonically decrease with height above the freezing level. Graupel with its relatively slow
398 fallspeeds (Fig. 4b) is carried aloft by the strong updrafts in the convective cores (Fig. 4a) where
399 its mass is maximized well above the freezing level. In contrast, the 4ICE simulations (Figs. 3e-
400 h) produce higher reflectivity values just above the freezing level due to higher fall speeds (Fig.
401 4c) that keep the peak hail mass nearer the freezing level as well as peak values that decrease
402 monotonically with height: both in good agreement with the observations. Profiles of peak
403 reflectivity within the model domain over the period 09 to 15 UTC (sampled to match the
404 observed squall line structure from 06 to 12 UTC, Fig. 5) show all three 3ICE simulations have a
405 pronounced low bias that ranges from about 5 dBZ below the freezing level to as much as 15
406 dBZ above the freezing level. The 4ICE simulations show a marked improvement in the bias at
407 almost all levels except for 4iceb lrg, which produces excessively large reflectivities (~15 dBZ)
408 near the melting level. The medium hail profile has the smallest overall bias and agrees best
409 with the observed. Though not quite as good, the smaller hail runs are significantly improved
410 over the 3ICE with a consistent low bias of just 5 dBZ at all levels.
411 Figure 6 shows statistical CFADs constructed over these same observed (06 to 12 UTC) and
412 model (09 to 15 UTC) time periods and domains. The observed CFAD shows higher
413 concentrations broadly ranging from 0 to 40 dBZ below the melting level; aloft a coherent core
414 of higher probabilities increases from 10 dBZ near 200 mb to 25 dBZ just above the freezing

415 level. Concentrations of infrequent but more intense echoes extend out to near 65 dBZ at and
416 below the freezing level, 50 dBZ at 12 km, and 40 dBZ at 16 km. None of the simulated 3ICE
417 CFADs (Figs. 6b-d) produce reflectivities over 50 dBZ above the freezing level and thus miss
418 the stronger echoes in the tail of the observed distribution consistent with Fig. 5. Furthermore,
419 the core of highest probabilities is either too broad with too many 40 dBZ echoes due to graupel
420 (3ice0), shifted too high with too many 30 dBZ echoes due to snow (3ice1), or shifted too low
421 with too many weak echoes (3ice3) compared to the NEXRAD data. In contrast, all of the 4ICE
422 simulations produce much better concentrations of both the moderate core echoes and the
423 infrequent but intense echoes that arise from hail relative to the observations (Figs. 6e-h). The
424 4ICE core distributions are still too broad as a result of too many weak echoes, but their overall
425 slope along on the right edge is fairly well aligned with the observed core probabilities.
426 The improvements in the 4ICE distributions are reflected in the normalized overlap score
427 between the observed and simulated PDFs at each level in the CFADs where unity represents
428 perfect overlap and zero no overlap. Figure 7 shows the 4ICE PDFs are consistently better than
429 the 3ICE above the freezing level from 6 to 10 km. Below the melting layer, all of the
430 simulations are similar and better than in the mixed and ice phase regions. The agreement
431 between the simulations and observations drops off sharply near storm top where simulated radar
432 echoes become too weak. This discrepancy was noted in L2011 and could be due to entrainment
433 effects wherein dry air disproportionately sublimates small particles while preserving relatively
434 large particles. Cloudsat CFADs show a distinct difference between convective and anvil
435 regions (Luo et al. 2009) with the highest probabilities in the anvil concentrated at the lowest
436 reflectivities, indicating mostly smaller particles, before shifting to higher values lower in the
437 cloud consistent with accretion and aggregation. In contrast, convective cloud top PDFs are

broader, indicating a mix of small and large particles, with a much great proportion of larger particles. The current model CFADs resemble the Cloudsat anvil distributions at upper levels.

b. LBA

Hail is associated with intense convection and as shown needed to produce stronger radar echoes. However, a key objective is for the 4ICE scheme to respond appropriately to the environment without the need for excessive tuning. The moderate intensity 23 February case is suitable for evaluating the new scheme for a weaker convective environment. A radar CAPPI for this case (Fig. 8a) shows the northern end of the transient convective line as it was starting to decay. Individual convective cells are loosely aligned with a small stratiform area extending northwestwards. The simulated convective leading edge using the 4ICE scheme (4iceb sml, Fig. 8b) is also cellular in nature and loosely organized into a north-south line with a small stratiform area extending northwestward, consistent with the weak southeast-northwest oriented shear on this day. A vertical east-west cross section (Fig. 8c) through the center of the domain shows the leading edge is somewhat multi-cellular (also see Fig. 10a) with a small, undeveloped stratiform area. Following L2011, a 64 x 64 km subdomain over the northern portion of the simulated line (dashed box in Fig. 8b) was used in the analyses with model data averaged to the 1-km resolution of the radar analyses. The mean convective fraction within this subdomain over the simulation period from 300 to 360 minutes using the 4ICE scheme ranged from 0.46 to 0.49 in close proximity to the radar value of around 0.4[3].

[3] As in L2007 and L2011, convective fractions were computed based on Rickenbach and Rutledge (1998), a texture algorithm applied to radar reflectivity data that largely follows Steiner et al. (1995) to match the radar observations.

459 Figure 9 shows time-height cross sections of peak reflectivity observed by the NCAR S-pol
460 radar within the dual-Doppler analysis domain and simulated within the model subdomains. As
461 previously noted (L2007; L2011), the original scheme (3ice0) with its excessive graupel
462 produces 40-dBZ echoes that penetrate much higher (over 12 km, Fig. 9b) than was observed (~7
463 km, Fig. 9a). Though better, 3ice1 (Fig. 9c), which eliminates the dry collection of ice/snow by
464 graupel (L2007), still produces excessive 40-dBZ echoes penetrations. The 40-dBZ echoes in
465 3ice3 (L2011) are greatly reduced aloft and closer to the observed, but 3ice3 results in an
466 elevated reflectivity maximum above the freezing level (Fig. 3d) that was not observed. None of
467 the 3ICE graupel simulations can reproduce the 45-dBZ echoes immediately above the freezing
468 level (~4.9 km) as was observed (Fig. 9a). In contrast, despite the addition of the higher density
469 frozen drops-hail ice class, none of the 4ICE simulations (Figs. 9e-h) produces the excessive 40-
470 dBZ echo penetrations in 3ice0 and 3ice1 and all can replicate the observed monotonically
471 decreasing reflectivity structure above the melting level though clearly the medium (4iceb med)
472 and larger (4iceb lrg) hail peak reflectivities that are too strong around the freezing level. These
473 results suggest that hail or frozen drops with their higher fall speeds (Fig. 10c) relative to graupel
474 (Fig. 10b) are crucial not detrimental for reproducing the observed core reflectivity structure of
475 even moderate convection. Peak reflectivity profiles from the 64 x 64 km model subdomains
476 over the final 60 minutes (Fig. 11) confirms the strong (nearly 15 dBZ) to moderate (~5 dBZ)
477 over bias in the 3ice0 and 3ice1 simulations aloft, respectively, as well as the under bias (~8
478 dBZ) in 3ice3 near the melting level, which contributes to the elevated maxima. The 4ICE
479 simulations with smaller hail clearly perform the best and show almost no bias (less than ~4
480 dBZ) through nearly the entire depth of the storm. Remarkably, none of the 4ICE runs produce
481 the over bias evident in runs 3ice0 and 3ice1 in the upper part of the storm, and all produce

482 monotonically decreasing profiles with height in agreement with the observations. However,
483 quite obviously the medium to larger hail sizes in runs 4iceb med and 4iceb lrg are much too
484 large, producing over biases of up to ~10 to 15 dBZ around the melting level. These results
485 suggest the new 4ICE scheme is quite capable of responding appropriately to the intensity of the
486 convective environment and can outperform the 3ICE-graupel scheme in terms of peak
487 reflectivities even in a moderate intensity environment. This actually is consistent with
488 polarimetric radar and wind profiler evidence that frozen drops or hail quite often are present in
489 tropical convection (Jameson et al. 1996; May et al. 2001); *in situ* aircraft data also confirmed
490 the presence of frozen drops in this case (Stith et al. 2002)

491 Simulated and observed radar CFADs (Fig. 12) also show the 4ICE scheme equals or
492 outperforms the 3ICE-graupel scheme in terms of overall reflectivity distributions for the
493 moderate 23 February case. The highest observed concentrations (Fig. 12a) gradually decrease
494 from between ~5 to 20 dBZ at and below the melting level (~4.9 km) to ~ -5 to 15 dBZ near
495 storm top with less apparent aggregation than MC3E (Fig. 6a). Low probabilities of moderately
496 strong echoes reach ~50 dBZ at and below the freezing level, 40 dBZ at ~7 km, and 30 dBZ at
497 12 km. As in MC3E only more pronounced, the original scheme (3ice0, Fig. 12b) produces
498 excessive concentrations of 20 to 40 dBZ echoes between the melting level and 10 km, and
499 again, though the number of excessive 30 to 40 dBZ echoes is reduced in 3ice1 (Fig. 12c), the
500 core of peak probabilities is ~10 dBZ too high. Core probabilities for 3ice3 are noticeably better
501 (Fig. 12d), but the amount of echoes too weak is higher as is the penetration of 20 to 30 dBZ
502 echoes near storm top. There is also an unphysical notch in the higher echo distribution just
503 above the freezing level. Though hail amounts are small in the 4ICE simulations, they dominate
504 the higher reflectivity values; the peak concentrations are nearly invariant (Figs. 12e-h) but are as

505 good as or better than the 3ICE at every level, aligning well with the observed concentrations
506 along 20 dBZ from the melting level to 12 km. In terms of echoes stronger than 20 dBZ in the
507 distribution tail, the smaller hail results (Figs. 12e-f) match the observed frequencies extremely
508 well while the medium (Fig. 12g) and larger hail (Fig. 12h) runs are overly intense especially
509 near the melting level. And as with MC3E, simulated probabilities collapse below 0 dBZ at
510 storm top and are ~10 dBZ weaker than observed.

511 The overall level-by-level performance is confirmed by the profiles of normalized PDF
512 matching scores (Fig. 13). From the freezing level to 10 km, the 3ice3 and 4ICE PDFs are all in
513 excellent agreement with the observed with matching scores on the order of 0.8, much better
514 than 3ice0 and 3ice1. Above 10 km, the performance of 3ice3 drops off quickly while the 4ICE
515 simulations continue to perform well up to 12 km before they begin to deviate from the observed
516 echo distributions near storm top. Below the melting level, the 3ICE and 4ICE schemes all
517 perform about the same and reasonably well with scores of around 0.75.

518

519 *c. Rainfall comparisons and validation*

520

521 In addition to radar reflectivity, the 4ICE scheme is validated with regard to surface rain rates.
522 Figures 14a,b show the instantaneous surface rain rates associated with the 4iceb sml simulations
523 shown in Figs. 2b and 8b for MC3E and LBA, respectively. Surface rain features in the
524 convective region are larger, better organized and more intense in MC3E; the stratiform region is
525 also larger and more coherent. Simulated surface rain rate histograms (Figs. 14c and d) can be
526 compared to observed rain rate histograms derived from the national Doppler radar network for
527 MC3E (Fig. 14c) and ground-based radar deployed for the LBA field campaign (Fig. 14d). The

528 3ICE and 4ICE histograms tend to fall into two distinct clusters, which is more apparent in the
529 MC3E case. For MC3E, the 3ICE simulations significantly underestimate the occurrence of
530 more intense rain rates in the tail of the distribution (Fig. 14c); the 4ICE histograms also
531 underestimate probabilities of extreme rain rates but are distinctly better than the 3ICE. For
532 LBA, the results are noisier due to a smaller sample size, but the overall results similar: both sets
533 of simulations underestimate the proportion of strongest rain rates but with the 4ICE simulations
534 closer to the observed histogram than the 3ICE. These results suggest the 4ICE simulations are
535 producing more realistic surface rain rate distributions than the 3ICE in each environment.
536
537 **4. Summary and conclusions**
538
539 The improved Goddard 3ICE 1M BMS based on Rutledge and Hobbs (L2011, cloud ice, snow
540 and graupel) was modified and hail processes added to produce an improved 1M 4ICE BMS
541 (cloud ice, snow, graupel, and frozen drops-hail) capable of more realistically simulating the
542 radar reflectivity patterns of intense and moderate convection better than previous 3ICE versions.
543 Hail processes taken from the 3ICE-hail scheme based on Lin et al. (1983) include hail riming,
544 accretion of rain, deposition/sublimation, melting, shedding and wet growth. Hail collection of
545 other ice species under dry growth conditions was eliminated to prevent the same excessive
546 buildup as had occurred with graupel (L2007); however, hail near wet growth is permitted to
547 collect other ice particles. Processes that freeze rain now initiate hail not graupel. Five new hail
548 processes were added: wet hail accretion of graupel, hail rime splintering, hail (also graupel)
549 conversion to snow via depositional growth at colder temperatures, hail conversion to graupel via
550 riming under non wet growth conditions, and wet graupel conversion to hail.

551 Besides adding the frozen drops-hail category, snow autoconversion was strengthened based
552 on the evidence of aggregation at colder temperatures (Field 1999), the collection efficiency of
553 cloud ice by snow increased, a water vapor diffusivity correction factor added, and a small
554 threshold introduced to prevent ice deposition growth into snow when ice is small. Maximum
555 ice supersaturation was increased to 20%, and cloud evaporation restricted to areas of subsidence
556 to mitigate spurious evaporation effects at cloud boundaries. Cloud ice can now persist in ice
557 sub-saturated conditions as commonly observed. Snow and graupel size mappings from L2011
558 were adjusted, including an increased aggregation effect for snow. A corresponding snow
559 density mapping was added (Brandes et al. 2007), and graupel divided into low and moderate
560 densities. Lastly, an SBM-based rain evaporation correction factor (Li et al. 2009) was added.
561 The new Goddard 4ICE scheme was used to simulate an intense continental squall line
562 observed during MC3E to evaluate its ability to simulate intense convection with significant hail
563 as well as a loosely-organized transient line of moderate convection from TRMM LBA to ensure
564 the scheme does not over predict less intense convection. For the intense squall line, the 4ICE
565 scheme with smaller and medium-sized hail, outperformed prior versions of the 3ICE-graupel
566 scheme in terms of peak reflectivities; larger hail produced excessively high values. Without
567 hail, the 3ICE-graupel versions could not generate reflectivities over 50 dBZ below freezing,
568 vastly underestimating the peak observed reflectivities throughout the depth of the storm with a
569 low bias near 15 dBZ at the freezing level, 10 dBZ at midlevels, and 5 to 15 dBZ at upper levels.
570 In contrast, the bias was significantly reduced in the 4ICE runs above the freezing level, except
571 for the strong over bias of 15 dBZ near the melting level for larger hail. For medium hail the
572 bias is less than 5 dBZ at almost all levels except for a positive bias of ~5 dBZ at the freezing
573 level. The smaller hail simulations produced a consistent low bias of just 5 dBZ at nearly every

574 level, still a noticeable improvement over the 3ICE graupel simulations. The 4ICE simulations
575 produced radar reflectivity CFADs in better agreement with observations (as reflected in their
576 normalized PDF overlapping scores) from 5 to 10 km with more realistic extremes in the
577 distribution tails and more realistic reflectivity structures above the freezing level with peak
578 reflectivities monotonically decreasing with height as observed versus the 3ICE graupel
579 simulations, which often produced elevated reflectivity maxima. Below the melting level, the
580 4ICE runs with smaller hail had peak reflectivities similar to the 3ICE. Those for medium and
581 larger hail were greater due to contributions from melting hail and were closer to the
582 observations for medium hail but not for larger where values were excessive. The agreement
583 between simulated and observed CFADs below the melting level was similar for all runs.
584 Overall, the 4ICE simulation with medium hail performed the best for the intense MC3E case.
585 For TRMM LBA, adding frozen drops/hail *per se* did not necessarily cause unrealistically
586 large reflectivity values[4]. While medium and larger hail did result in excessive peak
587 reflectivities by as much as 10 to 15 dBZ near the melting level, smaller hail had very small
588 biases (less than 5 dBZ) that were on average as good or better than the 3ICE versions at every
589 level. Small hail eliminated the over bias at middle and upper levels in the original and L2007
590 3ICE runs and outperformed the L2011 run above the freezing level by reproducing the observed
591 monotonic decrease with height and eliminating the unrealistic elevated reflectivity maxima.
592 The 4ICE simulations also produced radar CFADs whose normalized PDF scores were equal to
593 or superior to the 3ICE at all levels. The 4ICE simulations with smaller hail performed the best
594 overall for the moderate intensity LBA case.

[4] Trace amounts of mass first appear in the 4th ice class as frozen rain at ~10 m/s for the LBA cases and ~5 m/s for MC3E, but the sizes are very small and combined with the fact that reflectivity values take a while to grow strong shows that the 4ICE scheme is not predisposed to generating larger hail particles nor strong dBZs for every case.

595 Surface rainfall histograms were also used to evaluate the schemes for both cases with similar
596 results. In each case the 3ICE simulations significantly underestimated the occurrence of higher
597 rain rates compared to observed histograms while the 4ICE histograms had a noticeably higher
598 occurrence of stronger rain rates which were closer to but still less than the observed.
599 Though the bin rain evaporation correction (Li et al. 2009) did alter the temporal variation of
600 peak reflectivities, it had very little effect on either the peak reflectivity profiles or the model
601 CFADs in either case despite evidence that it reduced the intensity of the cold pool distribution
602 (see Fig. 15). The double cyclic lateral boundaries likely dampened its impact as initial
603 excessive evaporation without the correction could over moisten the sub-cloud layer and inhibit
604 successive over evaporation thus masking the effects of the correction. The LBA case was in a
605 moist environment and of short duration, which could also reduce the impact of the correction.
606 The 4ICE scheme with a frozen-drops hail category can simulate more intense radar echoes,
607 though choosing *a priori* the hail intercept for intense or moderate convection is not optimal. A
608 size-mapping scheme may alleviate the issue, but ultimately a multi-moment scheme is likely
609 needed. 4ICE also replicates the observed monotonic decrease in peak reflectivities with height
610 as a result of increasing the range of particle fall speeds to include the higher values associated
611 with frozen drops/hail, allowing a greater portion of their mass to remain near the freezing level.
612 The scheme also adds pathways (apparent processes) by which particles can move to other
613 categories due to their growth mechanisms. Hail can be rimed. If cloud freezes quickly, it
614 creates air pockets, which should lower hail density. Just as graupel is assumed to increase in
615 density and become hail when reaching wet growth, so too should hail density go down when
616 riming rates fall below wet growth. This is the basis for the new Primh hail riming to graupel
617 process. For the MC3E control case, Primh increases (decreases) the peak average graupel (hail)

618 content by 25% (5%), decreases the peak echoes by 3 dBZ at and above 12 km, and improves the
619 CFAD score by 2 to 4% from 4 to 13 km. The other new set of pathways relates to trace
620 amounts of graupel and hail that often persist aloft in the model long after convection ends.
621 Initially, sedimentation lowers their mass, but as the mass get small, with a fixed intercept, so
622 too do their fallspeeds. The result is tiny amounts of graupel and hail (mean volume diameters of
623 a few hundred microns or less) suspended over a broad area where they continue to grow from
624 deposition. The new Pvapg and Pvaph vapor conversion to snow processes reduce the area and
625 trace amounts of suspended graupel and hail but have minimal impact on the hail cores. For the
626 MC3E control case, peak reflectivity profiles are ~unchanged by Pvapg/Pvaph below 12.5 km
627 (the same is true for Primh below 9 km) as the collection of large amounts of super cooled water
628 dominates growth. Peak average snow, graupel and hail amounts increase ~5%, decrease 5%,
629 and increase 8%, respectively, when Pvapg/Pvaph are activated; Pvapg/Pvaph improve the
630 CFAD score by 2 to 5% from 4 to 11 km. The new apparent processes have a small effect on the
631 hail cores but allow the model to better address variations in particle density while slightly
632 improving the overall echo pattern.

633 Allowing a smooth transition in ice particle density (Morrison and Grabowski 2008) and
634 fallspeed coefficients (Lin and Colle 2011) is a recent and realistic addition to BMSs, though
635 comparisons with radar observations for intense cases are needed to evaluate their performance
636 and in contrast to having a separate hail category.

637 Ultimately, cases should be tested at higher resolution (100 m) to ensure the dynamics are well
638 resolved and not contributing to any biases. Further study is also needed to address the
639 abundance of weaker model dBZs near storm top to determine if this is an artifact of the radar
640 observations or the microphysics. Testing the 4ICE scheme in other environments using remote

641 sensing data for validation (Matsui et al. 2009) is important for systematically identifying and
642 eliminating any remaining biases. The ability to match the distribution and peak values of radar
643 reflectivities at all levels of a convective system is a fairly stringent test, but radar intensities are
644 not a unique solution and can arise from a variety of particle combinations. This is where *in situ*
645 aircraft observations could be very valuable in helping to further constrain the particle
646 characteristics. The next iteration of the Goddard scheme is planned to be 2M to ingest and
647 include the effects of aerosols and improve limitations inherent in 1M.
648
649 *Acknowledgements.* This research was supported by the NASA Precipitation Measurement
650 Missions (PMM), the NASA Modeling, Analysis, and Prediction (MAP) Program, and the Office
651 of Science (BER), U.S. Department of Energy/Atmospheric System Research (DOE/ASR)
652 Interagency Agreement No. DE-AI02-04ER63755. The authors are grateful to Drs. Ramesh
653 Kakar and David B. Considine at NASA headquarters for their support of this research, Dr.
654 Shaocheng Xie at Lawrence Livermore National Laboratory for providing the MC3E forcing
655 data, Dr. Robert Cifelli for providing the LBA radar data, Dr. Karen Mohr for discussions on
656 precipitation-surface flux interactions, and Drs. Toshihisa Matsui and Jainn J. Shi for
657 implementing and testing the 4ICE scheme in the Goddard satellite simulator and WRF,
658 respectively. We would also like to thank Dr. Jason Milbrandt and two other anonymous
659 reviewers for greatly helping us to improve the quality of the manuscript. Acknowledgment is
660 also made to the NASA Goddard Space Flight Center and NASA Ames Research Center
661 computing facilities and to Dr. Tsengdar Lee at NASA HQ for the computational resources used
662 in this research. MC3E is a NASA-DOE joint field campaign.
663

664 APPENDIX
665

666 *a. The hail budget equation*

667

668 The hail budget equation for the new 4ICE scheme is given as:

669 $$\frac{\partial q_h}{\partial t} = -V \bullet \nabla q_h - \frac{1}{\rho}\frac{\partial}{\partial z}\left((w - V_h) q_h \rho\right) + D_{qh} + Phfr + \left(1-\delta_3\right) Piacr + \left(1-\delta_3\right) \Pr aci + \left(1-\delta_2\right) Psacr$$

670

671 $$+\left(1-\delta_2\right) \Pr acs + Dgacr + \Pr acg + Dhacw + Dhacr + Whaci + Whacs + Whacg + Pg2h$$

672 $$+Phdep - Phsub - Pvaph - \Pr imh - Phmlt \qquad \text{(A1)}$$

673 where the first three terms on the RHS of Eq. A1 are the horizontal advection, vertical advection
674 and diffusion of hail, respectively, while $Phfr$ is the freezing of rain to hail, $Piacr$ cloud ice
675 accretion of rain, $\Pr aci$ rain accretion of cloud ice, $Psacr$ snow accretion of rain, $\Pr acs$ rain
676 accretion of snow, $Dgacr$ graupel accretion of rain, $\Pr acg$ rain accretion of graupel, $Dhacw$
677 hail riming, $Dhacr$ hail accretion of rain, $Whaci$, $Whacs$, and $Whacg$ wet hail accretion of
678 cloud ice, snow and graupel, respectively, $Pg2h$ the conversion of graupel to hail, $Phdep$ hail
679 deposition, $Phsub$ hail sublimation, $Pvaph$ the conversion of hail to snow via deposition,
680 $\Pr imh$ hail riming to graupel and $Phmlt$ hail melting. $Phfr$, $Dhacw$, $Dhacr$, $Whaci$, $Whacs$,
681 $Phdep$, $Phsub$, and $Phmlt$ follow the formulations of Lin et al. (1983), while $Piacr$, $\Pr aci$,
682 $Psacr$, $\Pr acs$, $Dgacr$, and $\Pr acg$ follow the formulations of Rutledge and Hobbs (1984).
683 $Whacg$ follows the Lin et al. (1983) formulation for $Whacs$ but using graupel instead of snow
684 parameters. Graupel is assumed to increase in density and become hail upon reaching wet
685 growth such that

$$Pg2h = \frac{q_g}{dt} \quad \text{at the moment when } Dgacw + Dgacr > Pgwet \tag{A2}$$

where the wet growth of graupel $Pgwet$ is computed using the formula for hail wet growth from Lin et al. (1983) but with graupel parameters[5].

Just as lower density particles can transition to a higher density class of particles, in the new 4ICE scheme, the reverse can occur. As such, when hail particles experience riming or deposition at colder temperatures, they are transitioned towards graupel and snow, respectively. For both processes, an increasing proportion of the mass of hail acquired via riming and deposition along with an equal portion of the previous hail mass is transferred to graupel and snow, respectively, using a sliding temperature scale with the proportion increasing with decreasing temperature. The conversion of hail to graupel via riming is thus formulated as:

$$\Pr imh = F_{rime} \times Dhacw \tag{A6}$$

where F_{rime} is given by $F_{rime} = 2.0 * \left(\frac{Tairc}{(t00 - t0)} \right)^2$ (A7)

where $Tairc$ is the air temperature in degrees Celcius, $t00$ is 238.16 degrees K, and $t0$ is 273.16 degrees K. Similarly the conversion of hail to snow via deposition is formulated as:

$$Pvaph = F_{vap} \times Phdep \quad \text{when the cloud water mixing ratio } q_c < 1.\text{e-}5 \text{ g/g} \tag{A8}$$

where F_{vap} uses the same temperature scaling as F_{rime}. The same form of the relation is used for the conversion of graupel to snow via deposition $Pvapg$. Although Hallet-Mossop rime splintering (Hallet and Mossop 1974) is not directly part of the hail equation, it does affect the hail riming term $Dhacw$ and is computed as:

[5] In nature, larger graupel particles would reach wet growth first. Converting only the mass above the mean volume diameter (0.5004) for the MC3E control case reduced the maximum average hail content by over 15%. However, peak reflectivities below 9 km were nearly unchanged due likely to high riming rates in the updraft cores but were decreased by 3 dBZ or more above 12 km.

$Pihmh = T_{fact} * Dhacw * 1000. * Xnsp \ln t * Xmsp \ln t$

where

$T_{fact} = 0.5$ when $-8^o C < Tairc < -2^o C$

$T_{fact} = 1.0$ when $-6^o C < Tairc < -4^o C$

where the peak number of ice splinters generated per milligram of rime $Xnsp \ln t = 370$ and the mass of each splinter $Xmsp \ln t = 4.4e^{-8}$ grams. $Pihmh$ is first subtracted directly from $Dhacw$. The water vapor diffusivity (D_v) in air was assumed to be a constant ($2.26e^{-5}$ m^2s^{-1}) in Rutledge and Hobbs (1984); it is parameterized as a function of temperature and pressure in this study following Massman (1998):

$$D_v = D_0 \left(\frac{T}{T_0} \right)^{1.81} \left(\frac{P_0}{P} \right),$$

where D_0 is the water vapor diffusivity ($2.18e^{-5}$ m^2s^{-1}) at T_0=273.15 K and P_0=1013.25 hPa. The importance of water vapor diffusivity on the diffusional growth rate of ice crystals as a function of pressure and temperature is illustrated in Fig. 9.4 of Rogers and Yau (1989). An adjustment factor (Fdwv) is used to adjust the diffusional growth rate of ice crystals based on a constant water vapor diffusivity.

b. Rain evaporation correction

The rain evaporation correction uses the empirical formula of Li et al. (2009):

$$r(q_r) = 0.11 q_r^{1.27} + 0.98 \quad \text{(A9)}$$

where r is the ratio of the rain evaporation rate between bulk and bin microphysics and q_r (g/kg) is the rain mixing ratio; r is based on cloud-resolving model simulations using both bulk and bin microphysics and can be used to scale down the bulk rain evaporation rate. In the new 4ICE scheme, the correction factor is made "physical" by scaling the rain intercept (i.e., increasing the grid local raindrop size) until the bulk rain evaporation rate matches the bin such that:

$$Ftnw = \left(\frac{1}{r}\right)^{3.35} \tag{A10}$$

where $Ftnw$ is the scaling factor for the rain intercept parameter.

c. Snow mapping

The snow mapping scheme maps the snow intercept parameter as a combination of variations in temperature and mixing ratio. Variations in mixing ratio are set for two distinct conditions: (1) at cold temperatures where aggregation effects are small, sizes are small and only slowly increase with increasing mixing ratio and (2) near the melting layer where aggregations effects are large, sizes are larger and size increases significantly with increasing mixing ratio. Another set of parameters controls how quickly the cold setting variations transform to the warm setting variations through the aggregation zone. For both cold and warm regions, an exponent is used to control the snow intercept; as this exponent approaches zero, snow sizes relax to those for a fixed snow intercept (i.e., larger sizes), and when the exponent approaches one, snow sizes collapse to that of a small base size. The formula for the snow size exponent is given by:

$$F_{\exp} = X_{sml} - X_{sml} \times \min\left(S_{\lim}, \max\left(0., \frac{(qs1 - sno1)}{dsno1}\right)^{s\exp 1}\right) \tag{A11}$$

which is then used create the mixing ratio component of the snow intercept scaling factor:

$$Ftnsq = \left(\frac{qs1}{S_{base}} \right)^{F\exp} \quad \text{(A12)}$$

where $qs1$ is the snow water content in g/m^3, and $Sno1$ is a snow water content threshold in g/m^3 above which snow sizes begin to increase. Snow sizes then continue to increase at an ever increasing rate over the next $dsno1$ g/m^3 until reaching the limit $S_{\lim}$. X_{sml} is arbitrarily given a number close to but less than one. This allows snow sizes to vary ever so slightly (i.e., not be a constant size) between snow contents of 0.0 and $Sno1$. The parameter settings for cold conditions transform through the snow aggregation zone (~ -20 to 0^o C) to those near 0^o C as:

$$P = Pwarm - \left(Pwarm - Pcold \right) \left(\frac{Tairc}{Tcold} \right)^{St\exp} \quad \text{(A13)}$$

where $Pwarm$ is the parameter value near the melting level, $Pcold$ the parameter value for cold conditions, and $Tcold$ the air temperature in degrees C for the cold parameter settings. An air temperature component for the snow intercept scaling factor, given by

$$FtnsT = \left(\exp\left(-1. \times Tslopes \times Tairc \right) \right)^{F\exp} \quad \text{(A14)}$$

where $Tslopes$ is the rate of snow intercept change with temperature on a natural logarithm scale and $Tairc$ is capped by $Tcold$, is then combined with the mixing ratio component of the snow intercept scaling factor to obtain the total snow intercept scaling factor:

$$Ftns = Ftnsq \times FtnsT \quad \text{(A15)}$$

with the condition that the snow size cannot go below a minimum value $D_{snowmin}$. The snow intercept mapping is combined with the Brandes et al. (2007) relation between snow density and median snow volume to get: $\rho_s = 0.001996 * \left(\frac{Ftns \times tns}{(qs \times \rho)} \right)^{0.2995}$ (A16)

where ρ_s is snow bulk density and tns the snow intercept. Table A1 lists the specific values used for the snow mapping.

REFERENCES

Bauer, P., 2001: Over-ocean rainfall retrieval from multisensor data of the Tropical Rainfall Measuring Mission (TRMM). Part I: Design and evaluation of inversion databases. *J. Atmos. Oceanic Technol*, **18,** 315–330.

Blossey, P. N., C. S. Bretherton, J. Cetrone, and M. Kharoutdinov, 2007: Cloud-resolving model simulations of KWAJEX: Model sensitivities and comparisons with satellite and radar observations. *J. Atmos. Sci.*, **64**, 1488–1508.

Braun, S. A., 2006: High-resolution simulation of Hurricane Bonnie (1998). Part II: Water budget. *J. Atmos. Sci.*, **63**, 43–64.

Brown, P. R., and H. A. Swann, 1997: Evaluation of key microphysical parameters in three-dimensional cloud-model simulations using aircraft and multiparameter radar data. *Quart. J. Roy. Meteor. Soc.*, **123,** 2245–2275.

Bryan, G. H., J. C. Wyngaard, J. M. Fritsch, 2003: Resolution requirements for the simulation of deep moist convection. *Mon. Wea. Rev.*, **131**, 2394–2416.

Chou, M.-D., and L. Kouvaris, 1991: Calculations of transmission functions in the IR CO_2 and O_3 Bands. *J. Geophys. Res.*, **96**, 9003-9012.

Chou, M.-D., W. Ridgeway, and M.-H. Yan, 1995: Parameterizations for water vapor IR radiative transfer in both the middle and lower atmospheres. *J. Atmos. Sci.*, **52**, 1159-1167.

Chou, M.-D., and M. J. Suarez, 1999: A shortwave radiation parameterization for atmospheric studies. 15, NASA/TM-104606, pp 40.

Chou, M.-D., K.-T. Lee, S.-C. Tsay, and Q. Fu, 1999: Parameterization for cloud longwave scattering for use in atmospheric models. *J. Climate*, **12**, 159-169.

Cifelli, R., W. A. Petersen, L. D. Carey, S. A. Rutledge, and M. A. F. da Silva Dias, 2002: Radar observations of the kinematic, microphysical, and precipitation characteristics of two MCSs in TRMM LBA. *J. Geophys. Res.*, **107**(D20), 8077, doi:10.1029/2000JD000264.

Cotton, W. R., G. J. Tripoli, R. M. Rauber, and E. A. Mulvihill, 1986: Numerical simulation of the effects of varying ice crystal nucleation rates and aggregation processes on orographic snowfall. *J. Climate Appl. Meteor.*, **25**, 1658–1680.

Diehl, K., and S. Wurzler, 2004: Heterogeneous Drop Freezing in the Immersion Mode: Model Calculations Considering Soluble and Insoluble Particles in the Drops. *J. Atmos. Sci.*, **61**, 2063–2072.

Diehl, K., M. Simmel, and S. Wurzler, 2006: Numerical sensitivity studies on the impact of aerosol properties and drop freezing modes on the glaciation, microphysics, and dynamics of clouds. *J. Geophys. Res.*, **111**, D07202, doi:10.1029/2005JD005884.

Eitzen, Z. A., and K.-M. Xu, 2005: A statistical comparison of deep convective cloud objects observed by an Earth Observing System satellite and simulated by a cloud-resolving model. *J. Geophys. Res.*, **110**, D15S14, doi:10.1029/2004JD005086.

Ferrier, B. S., 1994: A double-moment multiple-phase four-class bulk ice scheme. Part I: Description. *J. Atmos. Sci.*, **51,** 249–280.

Ferrier, B. S., W.-K. Tao, J. Simpson, 1995: A double-moment multiple-phase four-class bulk ice scheme. Part II: Simulations of convective storms in different large-scale environments and comparisons with other bulk parameterizations. *J. Atmos. Sci.*, **52**, 1001–1033.

Field, P. R., 1999: Aircraft observations of ice crystal evolution in an altostratus cloud. *J. Atmos. Sci.*, **56**, 1925–1941.

Fletcher, N. H., 1962: *The Physics of Rain Clouds*. Cambridge University Press, 386 pp.

Fu, Q., and K.-N. Liou, 1993: Parameterization of the radiative properties of cirrus clouds. *J. Atmos. Sci.*, **50**, 2008-2025.

Garrett, T. J., and Coauthors, 2005: Evolution of a Florida cirrus anvil. *J. Atmos. Sci.*, **62**, 2352–2372.

Grabowski, W. W., 1989: Numerical experiments on the dynamics of the cloud-environment interface: Small cumulus in a shear-free environment. *J. Atmos. Sci.*, **46,** 3513–3541.

Grabowski, W. W., P. K. Smolarkiewicz, 1990: Monotone finite-difference approximations to the advection-condensation problem. *Mon. Wea. Rev.*, **118**, 2082–2098.

Grabowski, W. W., and H. Morrison, 2008: Toward the mitigation of spurious cloud-edge supersaturation in cloud models. *Mon. Wea. Rev.*, **136**, 1224–1234.

Guy, N., X. Zeng, S. A. Rutledge, W.-K. Tao, 2013: Comparing the convective structure and microphysics in two Sahelian mesoscale convective systems: Radar observations and CRM simulations. *Mon. Wea. Rev.*, **141**, 582–601.

Hall, W. D., 1980: A detailed microphysical model within a two-dimensional dynamic framework: Model description and preliminary results. *J. Atmos. Sci.*, **37,** 2486–2507.

Hallet, J. and S. C. Mossop, 1974: Production of secondary ice particles during the riming process. *Nature*, **249,** 26–28.

Han, M., S. A. Braun, T. Matsui, and C. R. Williams (2013), Evaluation of cloud microphysics

schemes in simulations of a winter storm using radar and radiometer measurements, J. Geophys. Res. Atmos., **118**, 1401–1419, doi: 10.1002/jgrd.50115.

Hashino, T., and G. J. Tripoli, 2007: The Spectral Ice Habit Prediction System (SHIPS). Part I: Model description and simulation of the vapor deposition process. *J. Atmos. Sci.*, **64,** 2210–2237.

Heymsfield, A. J., 1982: A comparative study of the rates of development of potential graupel and hail embryos in high plains storms. *J. Atmos. Sci.*, **39,** 2867–2897.

Hong, S.-Y., J. Dudhia, and S.-H. Chen, 2004: A revised approach to ice microphysical processes for the bulk parameterization of clouds and precipitation. *Mon. Wea. Rev.*, **132**, 103-120.

Iguchi, T., T. Matsui, J. J. Shi, W.-K. Tao, A. P. Khain, A. Hou, R. Cifelli, A. Heymsfield, and A. Tokay, 2012a: Numerical analysis using WRF-SBM for the cloud microphysical structures in the C3VP field campaign: Impacts of supercooled droplets and resultant riming on snow microphysics, J. Geophys. Res., **117**, *D23206, doi:*10.1029/2012JD018101.

Iguchi, T., T. Matsui, A. Tokay, P. Kollias, and W.-K. Tao, 2012b: Two distinct modes in one-day rainfall event during MC3E field campaign: Analyses of disdrometer observations and WRF-SBM simulation, Geophys. Res. Lett., **39**, *L24805, doi:*10.1029/2012GL053329.

Jameson, A. R., M. J. Murphy, E. P. Krider, 1996: Multiple-parameter radar observations of isolated Florida thunderstorms during the onset of electrification. *J. Appl. Meteor.*, **35**, 343–354.

Jensen, E., O. Toon, S. Vay, J. Ovarlez, R. May, T. Bui, C. Twohy, B. Gandrud, R. Pueschel, and U. Schumann, 2001: Prevalence of ice- supersaturated regions in the upper troposphere: Implications for optically thin ice cloud formation. J. Geophys. Res., **106**(D15), 17253-17266.

Kessler, E., 1969: On the Distribution and Continuity of Water Substance in Atmospheric Circulations. Meteor. Monogr. No. 32, Amer. Meteor. Soc., 84 pp.

Khain, A. P. and I. Sednev, 1996: Simulation of precipitation formation in the eastern Mediterranean coastal zone using a spectral microphysics cloud ensemble model. *Atmos. Res.*, **43,** 77–110.

Khain, A. P., A. Pokrovsky, and I. Sednev, 1999: Some effects of cloud–aerosol interaction on cloud microphysics structure and precipitation formation: Numerical experiments with a spectral microphysics cloud ensemble model. *Atmos. Res.*, **52,** 195–220.

Khain, A. P., M. Ovtchinnikov, M. Pinsky, A. Pokrovsky, and H. Krugliak, 2000: Notes on the state-of-the-art numerical modeling of cloud microphysics. *Atmos. Res.*, **55,** 159–224.

Khain, A., M. Pinsky, M. Shapiro, A. Pokrovsky, 2001: Collision rate of small graupel and water drops. *J. Atmos. Sci.*, **58**, 2571–2595.

Khain, A. P., A. Pokrovsky, M. Pinsky, A. Seifert, and V. Phillips, 2004: Simulation of effects of atmospheric aerosols on deep turbulent convective clouds using a spectral microphysics mixed-phase cumulus cloud model. Part I: Model description and possible applications. *J. Atmos. Sci.*, **61,** 2963–2982.

Khairoutdinov, M., and D. Randall, 2006: High-resolution simulation of shallow-to-deep convection transition over land. *J. Atmos. Sci.*, **63**, 3421–3436.

Klaassen, G. P., and T. L. Clark, 1985: Dynamics of the cloud-environment interface and entrainment in small cumuli: Two-dimensional simulations in the absence of ambient shear. *J. Atmos. Sci.*, **42,** 2621–2642.

Klemp, J. B., and R. B. Wilhelmson, 1978: The simulation of three-dimensional convective storm dynamics. *J. Atmos. Sci.*, **35**, 1070-1096.

Kogan, Y. L., 1991: The simulation of a convective cloud in a 3-D model with explicit microphysics. Part I: Model description and sensitivity experiments. *J. Atmos. Sci.*, **48**, 1160–1189.

Kratz, D. P., M.-D. Chou, M. M.-H. Yan, C.-H. Ho, 1998: Minor trace gas radiative forcing calculations using the k-distribution method with one-parameter scaling. *J. Geophys. Res.*, **103**, 31647-31656.

Krueger, S. K., Q. A. Fu, K. N. Liou, and H. N. S. Chin, 1995: Improvements of an ice-phase microphysics parameterization for use in numerical simulations of tropical convection. *J. Appl. Meteor.*, **34,** 281–287.

Lang, S., W.-K. Tao, J. Simpson, and B. Ferrier, 2003: Modeling of convective–stratiform precipitation processes: Sensitivity to partitioning methods. *J. Appl. Meteor.*, **42**, 505–527.

Lang., S., W.-K. Tao, R. Cifelli, W. Olson, J. Halverson, S. Rutledge, and J. Simpson, 2007: Improving simulations of convective systems from TRMM LBA: Easterly and westerly regimes. *J. Atmos. Sci.*, **64**, 1141-1164.

Lang, S. E., W.-K. Tao, X. Zeng, and Y. Li, 2011: Reducing the biases in simulated radar reflectivities from a bulk microphysics scheme: Tropical convective systems. *J. Atmos. Sci.*, **68**, 2306–2320.

Lerach, D. G., S. A. Rutledge, C. R. Williams, and R. Cifelli, 2010: Vertical structure of convective systems during NAME 2004. *Mon. Wea. Rev.*, **138**, 1695–1714.

Li, X., W.-K. Tao, A. P. Khain, J. Simpson, D. E. Johnson, 2009: Sensitivity of a cloud-resolving model to bulk and explicit bin microphysical schemes. Part II: Cloud microphysics and storm dynamics interactions. *J. Atmos. Sci.*, **66**, 22–40.

Li, X., W.-K. Tao, T. Matsui, C. Liu, and H. Masunaga, 2010: Improving a spectral bin microphysical scheme using long-term TRMM satellite observations. *Quart. J. Roy. Meteoro. Soc.*, **136**, 382-399.

Li, Y., E. J. Zipser, S. K. Krueger, and M. A. Zulauf, 2008: Cloud-resolving modeling of deep convection during KWAJEX. Part I: Comparison to TRMM satellite and ground-based radar observations. *Mon. Wea. Rev.*, **136**, 2699-2712.

Lim, K.-S. S., and S.-Y. Hong, 2010: Development of an effective double-moment cloud microphysics scheme with prognostic cloud condensation nuclei (CCN) for weather and climate models. *Mon. Wea. Rev.*, **138**, 1587–1612.

Lin, C., 1999: Some bulk properties of cumulus ensembles simulated by a cloud-resolving model. Part I: Cloud root properties. *J. Atmos. Sci.*, **56**, 3724–3735.

Lin, Y.-L., R. D. Farley, and H. D. Orville, 1983: Bulk parameterization of the snow field in a cloud model. *J. Climate Appl. Meteor.*, **22**, 1065-1092.

Lin, Y., B. A. Colle, 2011: A new bulk microphysical scheme that includes riming intensity and temperature-dependent ice characteristics. *Mon. Wea. Rev.*, **139**, 1013–1035.

Luo, Y., R. Zhang, and H. Wang, 2009: Comparing occurrences and vertical structures of hydrometeors between eastern China and the Indian monsoon region using CloudSat/CALIPSO data. *J. Climate*, **22**, 1052–1064.

Massman, W. J., 1998: A review of the molecular diffusivities of H_2O, CO_2, CH_4, CO, O_3, SO_2, NH_3, N_2O, NO, and NO_2 in air, O_2, and N_2 near stp. *Atmos. Environ.*, **32**, 1111-1127.

Matsui, T., X. Zeng, W.-K. Tao, H. Masunaga, W. Olson, and S. Lang, 2009: Evaluation of long-term cloud-resolving model simulations using satellite radiance observations and multi-frequency satellite simulators. *J. Atmos. Ocn. Tech.*, **26,** 1261-1274.

May, P. T., A. R. Jameson, T. D. Keenan, P. E. Johnston, 2001: A comparison between polarimetric radar and wind profiler observations of precipitation in tropical showers. *J. Appl. Meteor.*, **40**, 1702–1717.

May, P. T., T. D. Keenan, 2005: Evaluation of microphysical retrievals from polarimetric radar with wind profiler data. *J. Appl. Meteor.*, **44**, 827–838.

Meyers, M. P., P. J. DeMott, and W. R. Cotton, 1992: New primary ice-nucleation parameterizations in an explicit cloud model. *J. Appl. Meteor.*, **31,**708–721.

Meyers, M. P., R. L. Walko, J. Y. Harrington, and W. R. Cotton, 1997: New RAMS cloud microphysics parameterization. Part II: The two-moment scheme. *Atmos. Res.*, **45,** 3–39.

Michalakes, J., J. Dudhia, D. Gill, T. Henderson, J. Klemp, W. Skamarock, and W. Wang, 2004: The Weather Research and Forecast Model: Software architecture and performance. The 11th ECMWF Workshop on the Use of High Performance Computing in Meteorology, 25–29 October 2004, Reading, U.K.

Milbrandt, J. A., and M. K. Yau, 2005a: A multimoment bulk microphysics parameterization. Part I: Analysis of the role of the spectral shape parameter. *J. Atmos. Sci.*, **62**, 3051–3064.

Milbrandt, J. A., and M. K. Yau, 2005b: A multimoment bulk microphysics parameterization. Part II: A proposed three-moment closure and scheme description. *J. Atmos. Sci.*, **62**, 3065–3081.

Milbrandt, J. A., and H. Morrison, 2013: Prediction of graupel density in a bulk microphysics scheme. *J. Atmos. Sci.*, **70**, 410–429.

Molthan, A. L., and B. A. Colle, 2012: Comparisons of single- and double-moment microphysics schemes in the simulation of a synoptic-scale snowfall event. *Mon. Wea. Rev.*, **140**, 2982–3002.

Morrison, H., J. A. Curry, V. I. Khvorostyanov, 2005: A new double-moment microphysics parameterization for application in cloud and climate models. Part I: Description. *J. Atmos. Sci.*, **62**, 1665–1677.

Morrison, H., and W. W. Grabowski, 2008: A novel approach for representing ice microphysics in models: Description and tests using a kinematic framework. *J. Atmos. Sci.*, **65**, 1528–1548.

Morrison, H., G. Thompson, and V. Tatarskii, 2009: Impact of cloud microphysics on the development of trailing stratiform precipitation in a simulated squall line: Comparison of one- and two-moment schemes. *Mon. Wea. Rev.*, **137**, 991–1007.

Muhlbauer, A., and coauthors, 2013: Reexamination of the state of the art of cloud modeling shows real improvements. *Bull. Amer. Meteor. Soc.*, **94**, ES45–ES48.

Ogura, Y., and N. A. Phillips, 1962: Scale analysis of deep and shallow convection in the atmosphere. *J. Atmos. Sci*., **19**, 173-179.

Olson, W.-S., C. D. Kummerow,, S. Yang, G. W. Petty, W.-K. Tao, T. L. Bell, S. A. Braun, Y. Wang, S. E. Lang, D. E. Johnson and C. Chiu, 2006: Precipitation and latent heating distributions from satellite passive microwave radiometry. Part I: Method and uncertainties. *J. Applied Meteor*., **45,** 702-720.

Ovtchinnikov, M., Y. L. Kogan, 2000: An investigation of ice production mechanisms in small cumuliform clouds using a 3D model with explicit microphysics. Part I: Model description. *J. Atmos. Sci.*, **57**, 2989–3003.

Panegrossi, G., S. Dietrich, F. S. Marzano, A. Mugnai, E. A. Smith, X. Xiang, G. J. Tripoli, P. K. Wang, and J. P. V. Poiares Baptista, 1998: Use of cloud model microphysics for passive microwave-based precipitation retrieval: Significance of consistency between model and measurement manifolds. *J. Atmos. Sci.*, **55**, 1644-1673.

Powell, S. W., R. A. Houze, Jr., A. Kumar, S. A. McFarlane, 2012: Comparison of simulated and observed continental tropical anvil clouds and their radiative heating profiles. *J. Atmos. Sci.*, **69**, 2662–2681.

Pruppacher, H. R., and J. D. Klett, 1980: *Microphysics of Clouds and Precipitation.* Reidel, 714 pp.

Randall, D., M. Khairoutdinov, A. Arakawa, and W. Grabowski, 2003: Breaking the cloud parameterization deadlock. *Bull. Amer. Meteor. Soc.*, **84**, 1547–1564.

Reisin, T., Z. Levin, and S. Tzivion, 1996: Rain production in convective clouds as simulated in an axisymmetric model with detailed microphysics. Part I: Description of the model. *J. Atmos. Sci.*, **53**, 497–519.

Reisner, J., R. M. Rasmussen, and R. T. Bruintjes, 1998: Explicit forecasting of supercooled liquid water in winter storms using the MM5 mesoscale model. *Quart. J. Roy. Meteor. Soc.*, **124,** 1071–1107.

Rickenbach, T. M., and S. A. Rutledge, 1998: Convection in TOGA COARE: Horizontal scale, morphology, and rainfall production. *J. Atmos. Sci.*, **55**, 2715-2729.

Rickenbach, T. M., R. N. Ferreira, J. B. Halverson, D. L. Herdies, and M. A. F. Silva Dias, 2002: Modulation of convection in the southwestern Amazon basin by extratropical stationary fronts. *J. Geophys. Res.*, **107**(D20), 8040, doi:10.1029/2000JD000263.

Rogers, R. F., M. L. Black, S. S. Chen, R. A. Black, 2007: An evaluation of microphysics fields from mesoscale model simulations of tropical cyclones. Part I: Comparisons with observations. *J. Atmos. Sci.*, **64**, 1811–1834.

Rogers, R. R., and M. K. Yau, 1989: *A short course in cloud physics 3rd Edition*, Pergamon press, 293pp.

Rutledge, S. A., and P. V. Hobbs, 1983: The mesoscale and microscale structure of organization of clouds and precipitation in midlatitude cyclones. VIII: A model for the "seeder-feeder" process in warm-frontal rainbands. *J. Atmos. Sci.*, **40**, 1185–1206.

Rutledge, S. A., and P. V. Hobbs, 1984: The mesoscale and microscale structure and organization of clouds and precipitation in midlatitude cyclones. Part XII: A diagnostic modeling study of precipitation development in narrow cold-frontal rainbands. *J. Atmos. Sci.*, **41**, 2949-2972.

Scott, B. C., and P. V. Hobbs, 1977: A theoretical study of the evolution of mixed-phase cumulus clouds. *J. Atmos. Sci.*, **34,** 812–826.

Seifert, A., and K. D. Beheng, 2006: A two-moment cloud microphysics parameterization for mixed-phase clouds. Part 1: Model description. *Meteor. Atmos. Phys.*, **92,** 45–66.

Skamarock, W. C., J. B. Klemp, J. Dudhia, D. Gill, D. Barker, M. Duda, X.-Y. Huang, W. Wang, and J. G. Powers, 2008: A description of the advanced research WRF Version 3. *NCAR Technical Note NCAR/TN-475+STR*, Boulder, Colorado.

Smedsmo, J. L., E. Foufoula-Georgiou, V. Vuruputur, F. Kong, K. Droegemeier, 2005: On the vertical structure of modeled and observed deep convective storms: Insights for precipitation retrieval and microphysical parameterization. *J. Appl. Meteor.*, **44**, 1866–1884.

Smith, P. L., Jr., C. G. Meyers, and H. D. Orville, 1975: Radar reflectivity factor calculations in numerical cloud models using bulk parameterization of precipitation. J. Appl. Meteor., 14, 1156-1165.

Smith, P. L., 1984: Equivalent radar reflectivity factors for snow and ice particles. J. Climate and Appl. Meteor., 23, 1258-1260.

Smolarkiewicz, P. K., 1983: A simple positive definite advection scheme with small implicit diffusion. *Mon. Wea. Rev*., **111**, 479-486.

Smolarkiewicz, P. K., 1984: A fully multidimensional positive definite advection transport algorithm with small implicit diffusion. *J. Comput. Phys.*, **54**, 325-362.

Smolarkiewicz, P. K., and W. W. Grabowski, 1990: The multidimensional positive advection transport algorithm: Nonoscillatory option. *J. Comput. Phys.*, **86**, 355-375.

Soong, S.-T., and Y. Ogura, 1980: Response of trade wind cumuli to large-scale processes. *J. Atmos. Sci.*, **37**, 2035-2050.

Starr, D. O'C., and S. K. Cox, 1985: Cirrus clouds. Part I: A cirrus cloud model. *J. Atmos. Sci.*, **42**, 2663-2681.

Steiner, M., R. A. Houze Jr., and S. E. Yuter, 1995: Climatological characteristics of three-dimensional storm structure from operational radar and rain gauge data. *J. Appl. Meteor*., **34**, 1978-2007.

Stevens, B., R. L. Walko, W. R. Cotton, G. Feingold, 1996: The spurious production of cloud-edge supersaturations by Eulerian models. *Mon. Wea. Rev.*, **124**, 1034–1041.

Stith, J. L., J. E. Dye, A. Bansemer, A. J. Heymsfield, C. A. Grainger, W. A. Petersen, and R. Cifelli, 2002: Microphysical observations of tropical clouds. J. Appl. Meteor., 41, 97-117.

Straka, J. M., E. R. Mansell, 2005: A bulk microphysics parameterization with multiple ice precipitation categories. *J. Appl. Meteor.*, **44**, 445–466.

Sui, C.-H., K.-M. Lau, and X. Li, 1998: Radiative-convective processes in simulated diurnal variations of tropical oceanic convection. *J. Atmos. Sci.*, **55**, 2345-2357.

Takahashi, T., 1976: Hail in an axisymmetric cloud model. *J. Atmos. Sci.*, **33,** 1579–1601.

Tao, W.-K., and J. Simpson, 1993: The Goddard Cumulus Ensemble Model. Part I: Model description. *Terrestrial, Atmospheric and Oceanic Sciences*, **4**, 19-54.

Tao, W.-K., J. Simpson, D. Baker, S. Braun, M.D. Chou, B. Ferrier, D. Johson, A. Khain, S. Lang, B. Lynn, C.-L Shie, D. Starr, Y. Wang, and P. Wetzel, 2003: Microphysics, radiation and surface processes in the Goddard Cumulus Ensemble (GCE) model. *Meteorol. Atmos. Phys.*, **82**, 97-137.

Tao, W.-K., and Coauthors, 2009: A multiscale modeling system: Developments, applications, and critical issues. *Bull. Amer. Meteor. Soc.*, **90**, 515–534.

Tao, W.-K., S. Lang, X. Zeng, X. Li, T. Matsui, K. Mohr, D. Posselt, J.-D. Chern, C. Peters-Lidard, P. Norris, I.-S. Kang, I. Choi, A. Hou, K.-M. Lau, and Y.-M. Yang, 2014: The Goddard Cumulus Ensemble model (GCE): Improvements and applications for studying precipitation processes. *Atmos. Res.*, (in review)

Thompson, G., P. R. Field, R. M. Rasmussen, W. D. Hall, 2008: Explicit forecasts of winter precipitation using an improved bulk microphysics scheme. Part II: Implementation of a new snow parameterization. *Mon. Wea. Rev.*, **136**, 5095–5115.

Van Weverberg, K., and Coauthors, 2013: The role of cloud microphysics parameterization in the simulation of mesoscale convective system clouds and precipitation in the tropical western pacific. *J. Atmos. Sci.*, **70**, 1104–1128.

Varble, A., A. M. Fridlind, E. J. Zipser, A. S. Ackerman, J.-P. Chaboureau, J. Fan, A. Hill, S. A. McFarlane, J.-P. Pinty, and B. Shipway (2011), Evaluation of cloud-resolving model intercomparison simulations using TWP-ICE observations: Precipitation and cloud structure, J. Geophys. Res., **116**, D12206, doi:10.1029/2010JD015180.

Waldvogel, A., B. Federer, P. Grimm, 1979: Criteria for the detection of hail cells. *J. Appl. Meteor.*, **18**, 1521–1525.

1172 Wang, Y., C. N. Long, L. R. Leung, J. Dudhia, S. A. McFarlane, J. H. Mather, S. J. Ghan, and X.
1173 Liu, 2009: Evaluating regional cloud-permitting simulations of the WRF model for the
1174 Tropical Warm Pool International Cloud Experiment (TWP-ICE), Darwin, 2006. J. Geophys.
1175 Res., **114**, D21203, doi:10.1029/2009JD012729.
1176
1177 Wisner, C., H. D. Orville, C. Myers, 1972: A numerical model of a hail-bearing cloud. *J.*
1178 *Atmos. Sci.*, **29**, 1160–1181.
1179
1180 Wu, D., X. Dong, B. Xi, Z. Feng, A. Kennedy, G. Mullendore, M. Gilmore, and W.-K. Tao,
1181 2013: Impacts of microphysical scheme on convective and stratiform characteristics in two
1182 high precipitation squall line events. J. Geophys.Res. Atmos., **118**, doi:10.1002/jgrd.50798.
1183
1184 Young, K. C., 1974: A numerical simulation of wintertime, orographic precipitation. I:
1185 Description of model microphysics and numerical techniques. *J. Atmos. Sci.,* **31,** 1735–1748.
1186
1187 Yuter, S. E., and R. A. Houze Jr., 1995: Three-dimensional kinematic and microphysical
1188 evolution of Florida cumulonimbus. Part II: Frequency distributions of vertical velocity,
1189 reflectivity, and differential reflectivity. *Mon. Wea. Rev.,* **123**, 1941–1963.
1190
1191 Zeng, X., W.-K. Tao, M. Zhang, C. Peters-Lidard, S. Lang, J. Simpson, S. Kumar, S. Xie, J. L.
1192 Eastman, C.-L. Shie, and J. V. Geiger, 2007: Evaluating clouds in long-term cloud-
1193 resolving model simulations with observational data. *J. Atmos. Sci.,* **64**, 4153-4177.
1194
1195 Zeng, X., W.-K. Tao, S. Lang, A. Hou, M. Zhang, and J. Simpson, 2008: On the sensitivity of
1196 atmospheric ensembles to cloud microphysics in long-term cloud-resolving model
1197 simulations. *J. Meteor. Soc. Japan*, **86A,** 45–65.
1198
1199 Zeng, X., W.-K. Tao, M. Zhang, A. Y. Hou, S. Xie, S. Lang, X. Li, D. Starr, X. Li, and J.
1200 Simpson, 2009: An indirect effect of ice nuclei on atmospheric radiation. *J. Atmos. Sci.*, **66,**
1201 41-61.
1202
1203 Zhang, M. H., J. L. Lin, R. T. Cederwall, J. J. Yio, and S. C. Xie, 2001: Objective analysis of
1204 ARM IOP data: Method and sensitivity. *Mon. Wea. Rev.,* **129,** 295–311.
1205
1206 Zhou, Y. P., W.-K. Tao, A. Y. Hou, W. S. Olson, C.-L. Shie, K.-M. Lau, M.-D. Chou, X. Lin
1207 and M. Grecu, 2007: Use of high-resolution satellite observations to evaluate cloud and
1208 precipitation statistics from cloud-resolving model simulations. Part I: South China Sea
1209 Monsoon experiment. *J. Atmos. Sci.,* **64**, 4309–4329.
1210
1211 Ziegler, C. L., 1985: Retrieval of thermal and microphysical variables in observed convective
1212 storms. Part 1: Model development and preliminary testing. *J. Atmos. Sci.*, **42**, 1487–1509.
1213
1214 Zipser, E. J., D. J. Cecil, C. Liu, S. W. Nesbitt, and D. P. Yorty, 2006: Where are the most
1215 intense thunderstorms on Earth? *Bull. Amer. Meteor. Soc.*, **87**, 1057-1071.
1216

1217

Table 1. Microphysical processes modified or added to the original (i.e., Tao and Simpson 1993; Tao et al. 2003) Goddard 1M Rutledge and Hobbs-based 3ICE-graupel bulk microphysics scheme (updated from L2011). Current changes associated with the new single-moment 4ICE scheme are shown in *italics*. New hail processes are in ***bold italics***. "f( )" indicates "function of". Esi, Egc, and Esc are the collection efficiencies of cloud ice by snow, cloud by graupel and cloud by snow, respectively. Qc0 is the cloud water threshold for snow riming, Qi0 the cloud ice threshold for snow autoconversion, ssi the supersaturation percentage with respect to ice, RH/RHice the relative humidity for water/ice, Dwv the water vapor diffusivity, Vs/g the snow/graupel fall velocity, Bh,i the immersion mode ice nucleating efficiency, IN the ice number concentration, and Tair the air temperature. Qr, Qi, Qs, Qg, and Qh are the rain, cloud ice, snow, graupel, and hail mixing ratios, respectively. The process nomenclature essentially follows Lin et al. (1983) and Rutledge and Hobbs (1983, 1984). ** =0 if ***Dhacw*** + ***Dhacr*** < *0.95* * ***Phwet.***

Process	Original	Modifications	Reference(s)/Notes
Psaut	Efficiency f(Tair)	Efficiency=0.15, Qi0 changed from g/g to g/m^{-3}, *time scale reduced from 1000 to 300 s, Qi0 lowered to 0.4 g m^{-3}, efficiency=0.25*	
Psaci	Esi = 0.1	Esi f(snow diameter), maximum Esi = 0.25, *maximum Esi=0.70, =0 when Qs=0*	See snow size mapping in Fig. 1

Praci/Piacr		Accounts for addition of cloud ice fall speed, *=0 when Qr=0, becomes hail not graupel*	Cloud ice fall speed follows Hong et al. (2004)
Pracw		*=0 when Qr=0*	
Psfi	Independent of RH	Depends on RH, accounts for cloud ice size via Meyers IN, which is a f(ssi), *added Dwv correction factor & Qi threshold*	Meyers et al. (1992); Krueger et al. (1995)
Psfw		*Added Dwv correction factor*	
Dgacs/Dgaci		Turned off	See Lang et al. (2007)
Dgacw	Egc=1.0	Egc is f(graupel diameter), maximum Egc = 0.65, *=0 when Qg=0*	See graupel size mapping in Fig. 1; Khain et al. (2001)
Dgacr/Pracg		*=0 when Qg=0 or Qr=0*	

Psacw/Pwacs	Esc=1.0, Qc0=0.5 g/kg	Esc=0.45, Qc0=1.0 g/kg, *Qc0=0.5 g/kg, =0 if Qs=0*	Lang et al. (2007); Morrison and Grabowski (2008)
Pracs/Psacr		*=0 if Qr or Qs=0, =hail not graupel*	
Rime Splintering	None	Added and applied to Psacw/Pgacw, not f(Vs/g) or f(cloud size), *added for* ***Dhacw***	Hallet and Mossop (1974); f(Tair) and splinter mass follow Ferrier (1994)
Pidw/Pidep	Based on Fletcher	Based on Meyers IN, which is a f(ssi), *added Dwv correction factor to Pidep*	Fletcher (1962); Meyers et al. (1992)
Pint	Based on Fletcher	Based on Meyers IN, which is a f(ssi), previous ice concentration checked	Fletcher (1962); Meyers et al. (1992)
Immersion Freezing	None	Added based on Diehl	Diehl and Wurzler (2004); Diehl et al. (2006), assumes Bh,i = 1.01 e-2 for pollen

Contact Nucleation	None	Added based on Cotton and Pruppacher for Brownian diffusion only	Cotton et al. (1986); Pruppacher and Klett (1980), 500 active nuclei per cc with radii of 0.1 microns
Saturation Adjustment	Sequential based on Tao	Modified sequential, iterative, ssi up to 10%, *ssi up to 15% ($T<-44^oC$) and 20% ($T>-38^oC$), no evaporation if W > -0.1 m/s, no sublimation if RHice > 70% or W > 0 m/s*	Tao et al. (2003) *Reisner (personal)*
Psdep/Pgdep		=0 if Qs/Qg=0	
Snow/Graupel Sublimation	None	Allowed if outside cloud and air subsaturated, *allowed if air subsaturated*	
*Pvapg/**Pvaph***		*convert Qg/Qh to Qs via deposition if Qc < 1.e-5 g/g, f(Tair)*	
Snow/ Graupel	Based on fixed	Based on intercepts mapped according to snow/graupel mass and Tair, *revised,*	

size	intercepts	*greater aggregation effect for snow*	
Snow density	=0.1 g cm^{-3}	=0.05 g cm^{-3}, *f(snow size)*	*Brandes et al. (2007)*
Graupel density	=0.4 g cm^{-3}	*=0.3 g cm^{-3} if Qg < 2.0 g m^{-3}* *=0.5 g cm^{-3} if Qg > 2.0 g m^{-3}*	*Brown and Swann (1997);* *Straka and Mansell 2005*
Cloud ice fall Speed	None or Starr and Cox	Based on Hong, *included in all sweep volumes*	Hong et al. (2004); Starr and Cox (1985)
Ern		*Added rain evaporation correction via tnw, max correction=1.30, Added Dwv correction factor*	*Li et al. (2009)*
Pmlts/Pmltg		*Added Dwv correction factor*	
Whaci		*Added from Lin, =0 if Qh=0,*	*Lin et al. (1983)*
Whacs		*Added from Lin, =0 if Qh/Qs=0*	*Lin et al. (1983)*
Whacg		*Follows **Whacs**, =0 if Qh/Qg=0*	
Dhacw		*Added from Lin, =0 if Qh=0*	*Lin et al. (1983)*

Primh	*convert Qh to Qg via riming,*	*see text on Milbrandt*
	*f(**Phwet**, Tair)*	*and Morrison (2013)*
Dhacr	*Added from Lin, =0 if Qh/Qr=0*	*Lin et al. (1983)*
Phwet	*Added from Lin, =0 if Qh=0*	*Lin et al. (1983)*
Phfr	*Follows Pgfr but frozen rain*	*Rutledge and Hobbs (1984)*
	= hail not graupel, =0 if Qr=0	
Phdep	*Added from Lin, =0 if Qh=0*	*Lin et al. (1983)*
Phmlt/ Whacr	*Added from Lin*	*Lin et al. (1983)*

Table 2. Numerical experiments performed for both the 20 May 2012 MC3E and 23 February 1999 TRMM LBA cases using various options of the Goddard 1M bulk microphysics scheme where N_0h is the hail intercept.

Experiment	Description	Reference(s)/Notes
3ice0	3ICE graupel (original)	Rutledge and Hobbs (1983, 1984)
3ice1	Original + no graupel dry collection	Lang et al. (2007)
3ice3	Original + no graupel dry collection + snow/graupel size mapping	Lang et al. (2011)
4ice sml	New 4ICE with smaller hail	$N_0h = 0.0200$ cm^{-4}
4iceb sml	New 4ICE with smaller hail + rain evaporation correction	$N_0h = 0.0200$ cm^{-4}
4iceb med	New 4ICE with medium hail + rain evaporation correction	$N_0h = 0.0020$ cm^{-4}
4iceb lrg	New 4ICE with larger hail + rain evaporation correction	$N_0h = 0.0002$ cm^{-4}

Table A1. Values of snow intercept mapping parameters used to obtain the characteristic snow size mapping shown in Fig 1e.

Snow Mapping Parameter	Cold Value	Warm Value	Value
Tcold			-25 ^{o}C
Twarm			0 ^{o}C
*sno*1	1.0 g m^{-3}	0.0 g m^{-3}	
*dsno*1	4.0 g m^{-3}	1.0 g m^{-3}	
s exp1	1.1	0.6	
S_{lim}			0.8
X_{sml}			0.97
S_{base}			0.040 g m^{-3}
st exp1			0.5
tns			0.10 cm^{-4}
Tslopes (cm^{-4} C^{-1})			0.1842

1388
1389 FIGURE CAPTIONS

1390

1391 Figure 1. Characteristic sizes (inverse of the slope parameter) of precipitation ice particle
1392 distributions (inverse exponential) as a function of precipitation ice content and temperature for
1393 (a) snow in the original Rutledge and Hobbs (1983,1984)-based Goddard scheme, (b) graupel in
1394 the original Goddard scheme, (c) snow in the modified Goddard 3ICE scheme, (d) graupel in the
1395 modified Goddard 3ICE scheme, (e) snow in the new Goddard 4ICE scheme, (f) graupel in the
1396 new Goddard 4ICE scheme, and (g) snow density in the new Goddard 4ICE scheme. (a) – (d)
1397 adapted from L2011.

1398

1399 Figure 2. Horizontal cross sections of radar reflectivity for the 20 May 2011 MC3E case (a)
1400 observed by the NEXRAD Doppler radar network at 10:30 UTC over north-central Oklahoma
1401 (figure obtained from the National Mosaic and Next Generation Quantitative Precipitation
1402 Estimation) and (b) simulated using the new 4ICE scheme with smaller hail and bin rain
1403 evaporation correction (4iceb sml) at a simulation time of 85.5 h (13:30 UTC). The vertical east-
1404 west cross section of radar reflectivity shown in (c) was taken through the center of the domain
1405 from the same simulation and time as (b).

1406

1407 Figure 3. Time-height cross sections of maximum radar reflectivity for the 20 May 2011 MC3E
1408 case (a) observed by NEXRAD Doppler radar and simulated using the (b) original 3ICE, (c)
1409 level 1 improved 3ICE, (d) level 3 improved 3ICE, (e) new 4ICE with smaller hail, (f) new 4ICE
1410 with smaller hail and bin rain evaporation correction, (g) new 4ICE with moderate hail and bin
1411 rain evaporation correction, and (h) new 4ICE with larger hail and bin rain evaporation

correction Goddard microphysics scheme. Right axes are heights in km, while horizontal dashed lines show the level of indicated environmental temperatures in degrees C. Times range from 00 UTC 20 May to 00 UTC 21 May 2011.

Figure 4. Same as Fig. 2c except showing vertical cross sections of simulated (a) vertical velocities (b) graupel fall speeds, and (c) hail fall speeds.

Figure 5. Vertical profiles of maximum radar reflectivity for the 20 May 2011 MC3E case extracted between 06 and 12 UTC from Doppler radar observations and between 09 and 15 UTC from the three Goddard 3ICE simulations and four Goddard 4ICE simulations shown in Figure 2.

Figure 6. Radar reflectivity CFADs for the 20 May 2011 MC3E case constructed from (a) NEXRAD Doppler radar observations and simulations using the (b) original 3ICE, (c) level 1 improved 3ICE, (d) level 3 improved 3ICE, (e) new 4ICE with smaller hail, (f) new 4ICE with smaller hail and bin rain evaporation correction, (g) new 4ICE with moderate hail and bin rain evaporation correction, and (h) new 4ICE with larger hail and bin rain evaporation correction Goddard microphysics scheme. Heavy thick lines in (b) - (h) show the edges of the core observed frequency probabilities [i.e., the 5 % contours shown in (a)] and the outer limits of the observed frequency distributions [i.e., the 0 % contours shown in (a)]. Right axes are heights in km, while horizontal dashed lines show the level of indicated environmental temperatures in degrees C.

1434 Figure 7. Vertical profiles of PDF matching scores (i.e., the amount of overlap between the
1435 simulated and observed PDF at each level) for the 20 May 2011 MC3E simulations using the (b)
1436 original 3ICE, (c) level 1 improved 3ICE, (d) level 3 improved 3ICE, (e) new 4ICE with smaller
1437 hail, (f) new 4ICE with smaller hail and bin rain evaporation correction, (g) new 4ICE with
1438 moderate hail and bin rain evaporation correction, and (h) new 4ICE with larger hail and bin rain
1439 evaporation correction Goddard microphysics scheme.
1440
1441 Figure 8. Horizontal cross sections of radar reflectivity for the 23 February 1999 LBA case (a)
1442 observed by the S-Pol radar at 20:50 UTC over Amazonia overlaid with storm-relative winds
1443 from a dual-Doppler wind analysis and the track of the University of North Dakota Citation
1444 aircraft (figure adapted from http://radarmet.atmos.colostate.edu/lba_trmm/23feblba_cappi.html
1445 and Lang et al. 2007) and (b) simulated using the new 4ICE scheme with smaller hail and bin
1446 rain evaporation correction (4iceb sml) at a simulation time of 330 minutes (21:00 UTC). The
1447 vertical east-west cross section of radar reflectivity shown in (c) was taken through the center of
1448 the domain from the same simulation and time as (b). The solid rectangle and dashed box shown
1449 in (b) denote the north-south oriented rectangular patch of higher sensible/lower latent heat
1450 fluxes (Ji Parana) imposed to initiate convection and the analysis domain, respectively.
1451
1452 Figure 9. Time-height cross sections of maximum radar reflectivity for the 23 February 1999
1453 LBA case (a) observed by the S-pol ground-based radar and simulated using the (b) original
1454 3ICE, (c) level 1 improved 3ICE, (d) level 3 improved 3ICE, (e) new 4ICE with smaller hail, (f)
1455 new 4ICE with smaller hail and bin rain evaporation correction, (g) new 4ICE with moderate hail
1456 and bin rain evaporation correction, and (h) new 4ICE with larger hail and bin rain evaporation

1457 correction Goddard microphysics scheme. Right axes are heights in km, while horizontal dashed
1458 lines show the level of indicated environmental temperatures in degrees C. Model data were
1459 taken from a 64 km x 64 km subdomain. Black and gray labels at the bottom of (a) are the UTC
1460 and approximate matching times, respectively.
1461
1462 Figure 10. Same as Fig. 8c except showing vertical cross sections of simulated (a) vertical
1463 velocities (b) graupel fall speeds, and (c) hail fall speeds.
1464
1465 Figure 11. Vertical profiles of the maximum radar reflectivity for the 23 February 1999 LBA
1466 case extracted from the S-pol radar observations and the last 60 minutes of the three Goddard
1467 3ICE simulations and four Goddard 4ICE simulations shown in Figure 6. Model data were taken
1468 from a 64 km x 64 km subdomain.
1469
1470 Figure 12. Radar reflectivity CFADs for the 23 February 1999 LBA case constructed from (a) S-
1471 pol radar observations and the final 60 minutes of the simulations using the (b) original 3ICE, (c)
1472 level 1 improved 3ICE, (d) level 3 improved 3ICE, (e) new 4ICE with smaller hail, (f) new 4ICE
1473 with smaller hail and bin rain evaporation correction, (g) new 4ICE with moderate hail and bin
1474 rain evaporation correction, and (h) new 4ICE with larger hail and bin rain evaporation
1475 correction Goddard microphysics scheme. Heavy thick lines in (b) - (h) show the edges of the
1476 core observed frequency probabilities [i.e., the 5 % contours shown in (a)] and the outer limits of
1477 the observed frequency distributions [i.e., the 0 % contours shown in (a)]. Right axes are heights
1478 in km, while horizontal dashed lines show the level of indicated environmental temperatures in
1479 degrees C. Model data were taken from a 64 km x 64 km subdomain.

1480

1481 Figure 13. Vertical profiles of PDF matching scores for the 23 February 1999 LBA simulations
1482 over the final 60 minutes using the (b) original 3ICE, (c) level 1 improved 3ICE, (d) level 3
1483 improved 3ICE, (e) new 4ICE with smaller hail, (f) new 4ICE with smaller hail and bin rain
1484 evaporation correction, (g) new 4ICE with moderate hail and bin rain evaporation correction, and
1485 (h) new 4ICE with larger hail and bin rain evaporation correction Goddard microphysics scheme.
1486 Model data were taken from a 64 km x 64 km subdomain.

1487

1488 Figure 14. Instantaneous surface rainfall rates corresponding to the horizontal radar reflectivity
1489 cross sections shown for the 20 May MC3E case in Fig. 2b (a) and the 23 February LBA case in
1490 Fig. 8b (b). (c) surface rainfall histograms observed by the Doppler radar network around the
1491 MC3E sounding array from 06-12 UTC and simulated with Goddard microphysics from 09-15
1492 UTC for the 20 May MC3E case. (d) surface rainfall histograms derived from ground-based
1493 radar observations collected from 2002-2130 UTC and simulated over the final 60 minutes of
1494 simulation time over a 64 km x 64 km subdomain (shown by the dashed square in panel b) for
1495 the 23 February 1999 case using the Goddard microphysics schemes.

1496

1497 Figure 15. Distribution of surface cold pool intensities for the 20 May MC3E case for the
1498 smaller hail runs with and without the bin rain evaporation correction, 4iceb sml and 4ice sml,
1499 respectively. Intensities are shown in terms of the surface potential temperature deviations (K)
1500 over the 09 to 15 UTC analysis period for regions where the lowest level rain mixing ratio
1501 exceeds 0.1 g m^{-3}.

1502

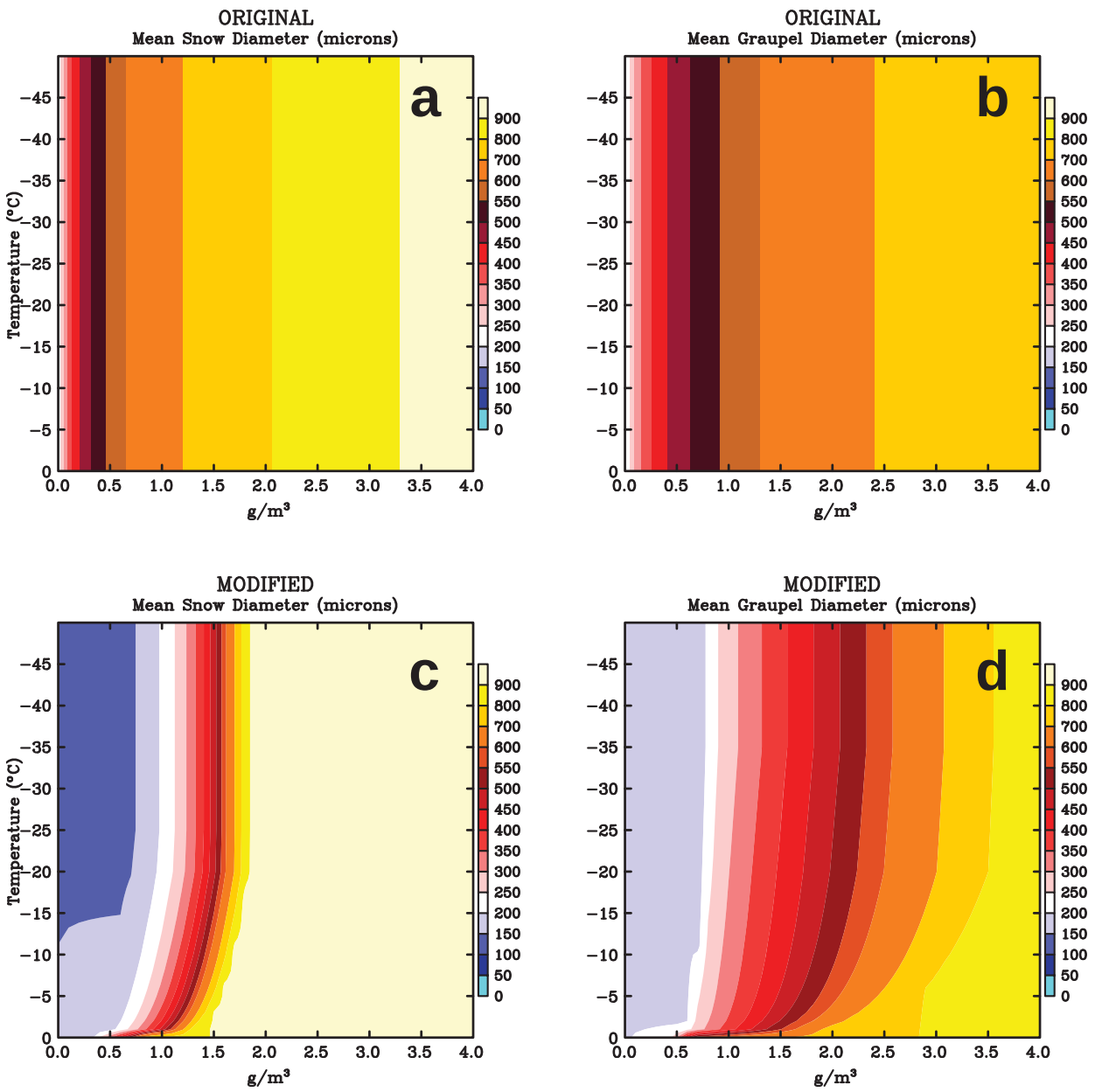
ORIGINAL
Mean Snow Diameter (microns)
a
ORIGINAL
Mean Graupel Diameter (microns)
b
MODIFIED
Mean Snow Diameter (microns)
c
MODIFIED
Mean Graupel Diameter (microns)
d
Temperature (°C)
g/m³
0.0 0.5 1.0 1.5 2.0 2.5 3.0 3.5 4.0
0 −5 −10 −15 −20 −25 −30 −35 −40 −45
900 800 700 600 550 500 450 400 350 300 250 200 150 100 50 0

1542
1543
1544
1545

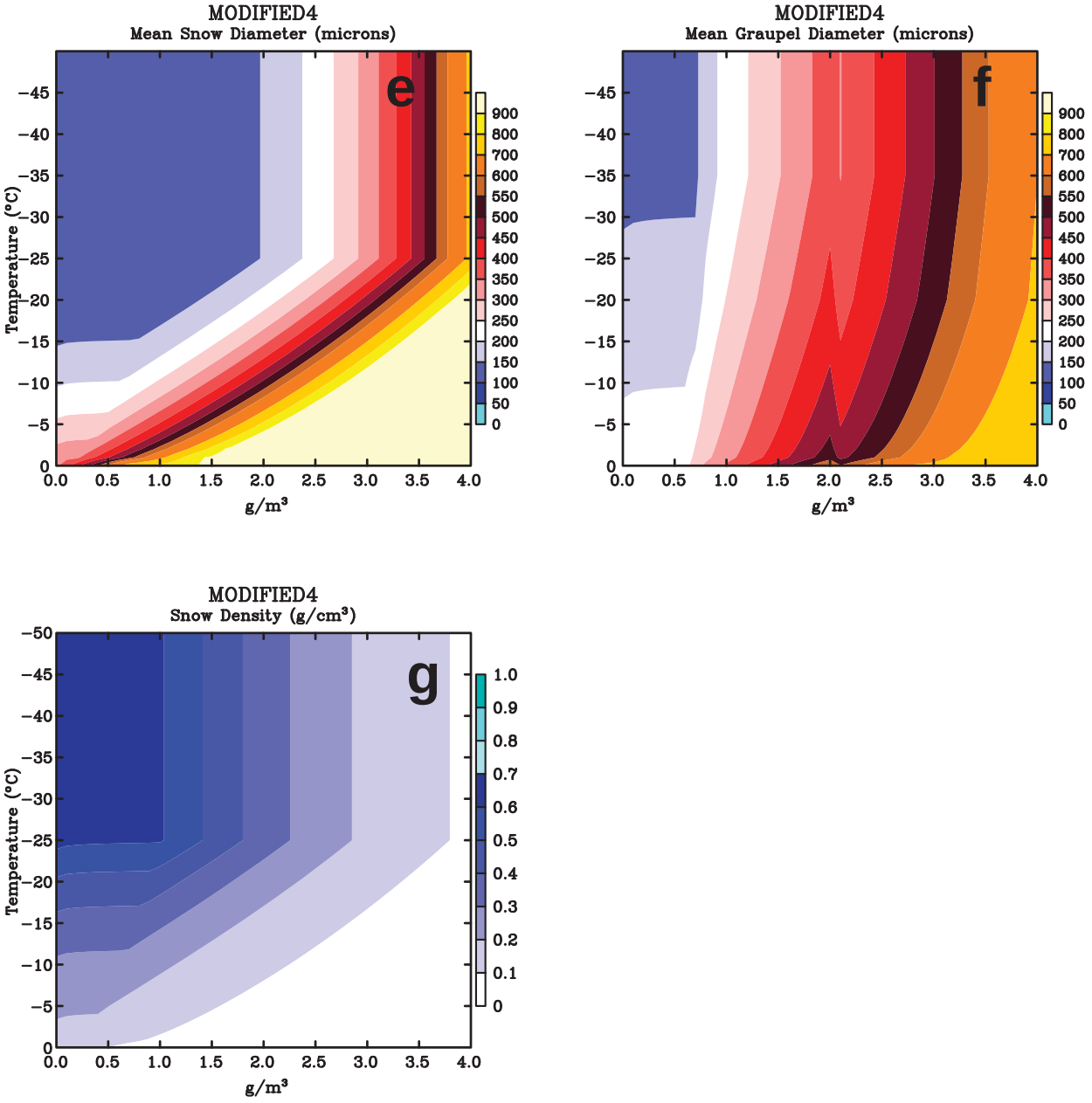

Figure 1. Characteristic sizes (inverse of the slope parameter) of precipitation ice particle distributions (inverse exponential) as a function of precipitation ice content and temperature for (a) snow in the original Rutledge and Hobbs (1983,1984)-based Goddard scheme, (b) graupel in the original Goddard scheme, (c) snow in the modified Goddard 3ICE scheme, (d) graupel in the modified Goddard 3ICE scheme, (e) snow in the new Goddard 4ICE scheme, (f) graupel in the new Goddard 4ICE scheme, and (g) snow density in the new Goddard 4ICE scheme. (a) – (d) adapted from L2011.

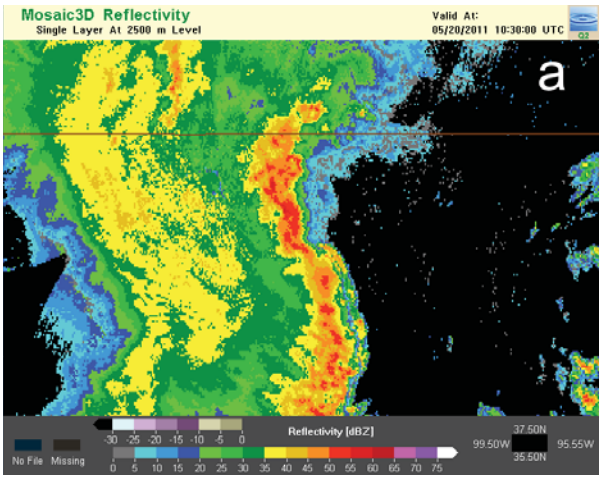

1553
1554

1555

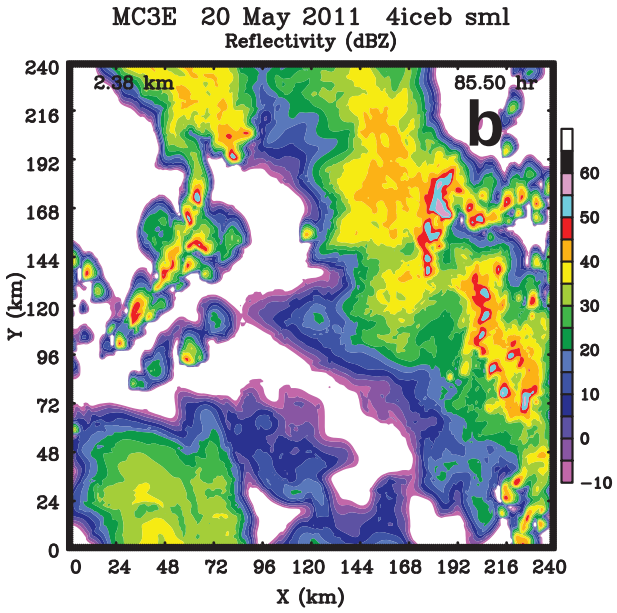

1556

1557
1558

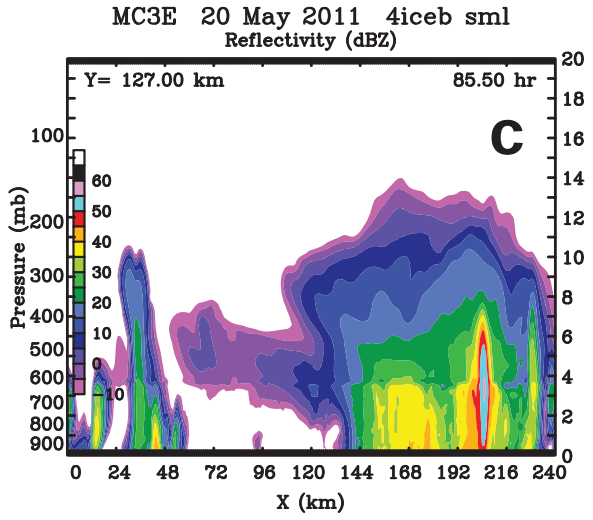

Figure 2. Horizontal cross sections of radar reflectivity for the 20 May 2011 MC3E case (a) observed by the NEXRAD Doppler radar network at 10:30 UTC over north-central Oklahoma (figure obtained from the National Mosaic and Next Generation Quantitative Precipitation Estimation) and (b) simulated using the new 4ICE scheme with smaller hail and bin rain evaporation correction (4iceb sml) at a simulation time of 85.5 h (13:30 UTC). The vertical east-west cross section of radar reflectivity shown in (c) was taken through the center of the domain from the same simulation and time as (b).

1567
1568
1569
1570
1571

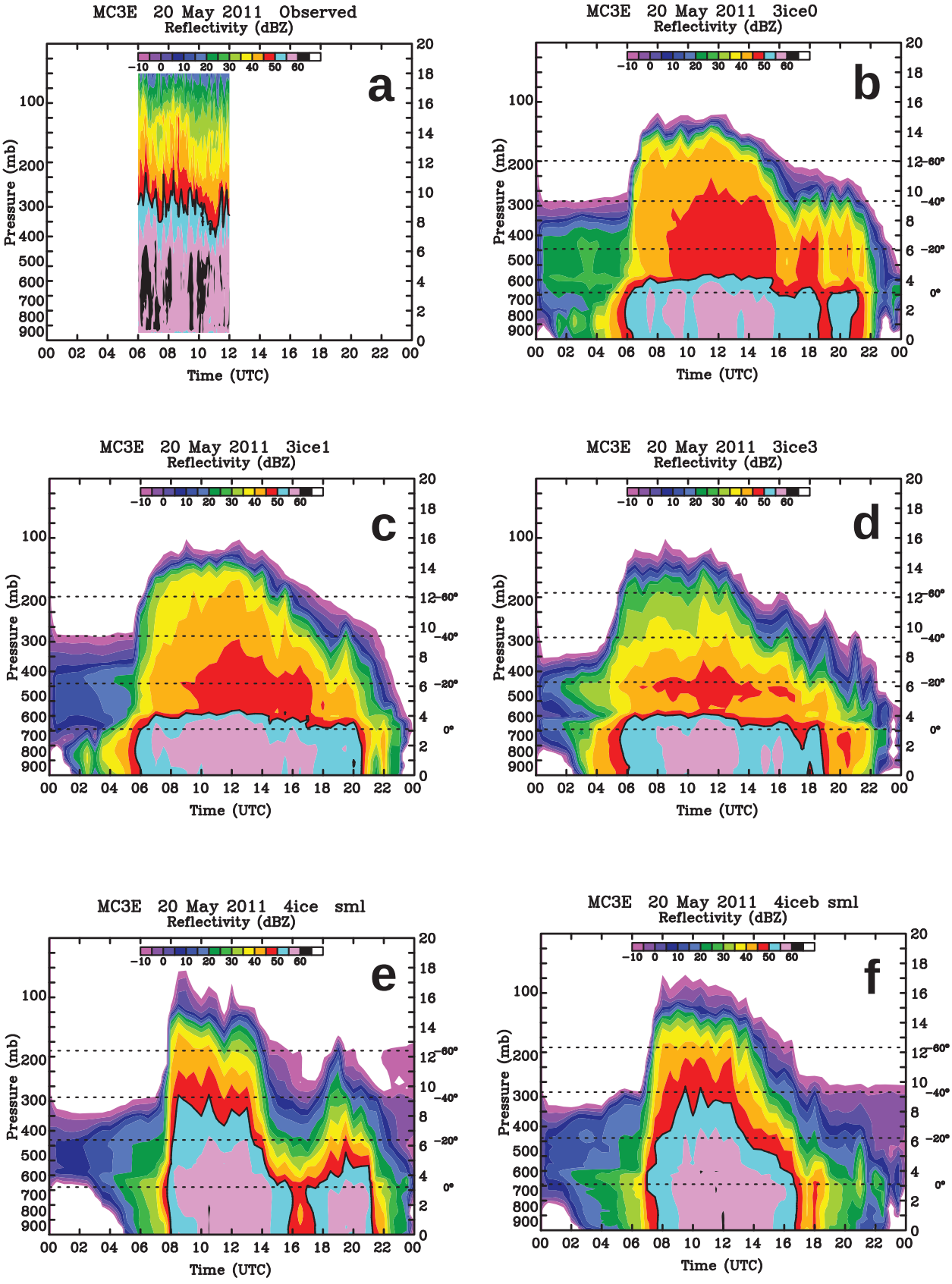

1572

1573

1574

1575

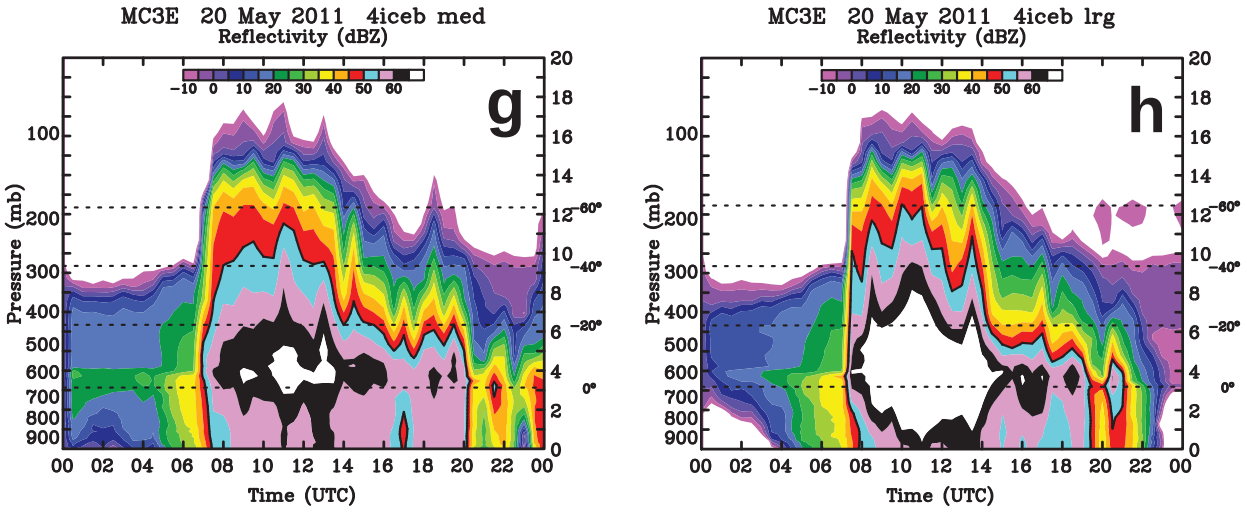

Figure 3. Time-height cross sections of maximum radar reflectivity for the 20 May 2011 MC3E case (a) observed by NEXRAD Doppler radar and simulated using the (b) original 3ICE, (c) level 1 improved 3ICE, (d) level 3 improved 3ICE, (e) new 4ICE with smaller hail, (f) new 4ICE with smaller hail and bin rain evaporation correction, (g) new 4ICE with moderate hail and bin rain evaporation correction, and (h) new 4ICE with larger hail and bin rain evaporation correction Goddard microphysics scheme. Right axes are heights in km, while horizontal dashed lines show the level of indicated environmental temperatures in degrees C. Times range from 00 UTC 20 May to 00 UTC 21 May 2011.

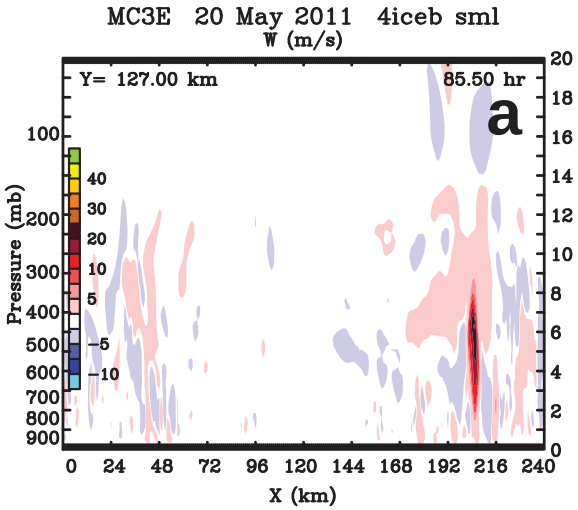
MC3E 20 May 2011 4iceb sml
W (m/s)
Y= 127.00 km
85.50 hr
a
Pressure (mb)
X (km)

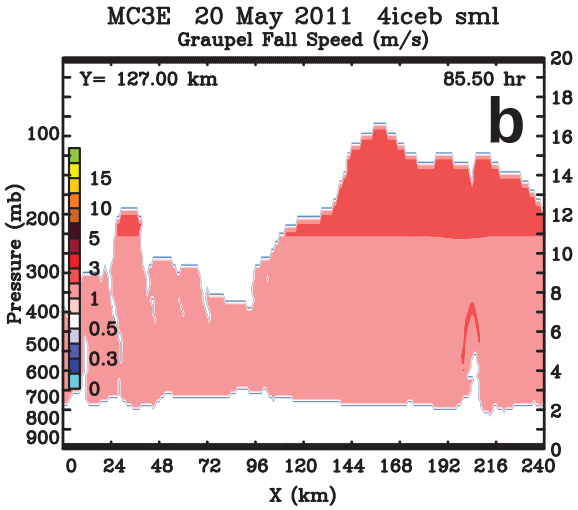
MC3E 20 May 2011 4iceb sml
Graupel Fall Speed (m/s)
Y= 127.00 km
85.50 hr
b
Pressure (mb)
X (km)

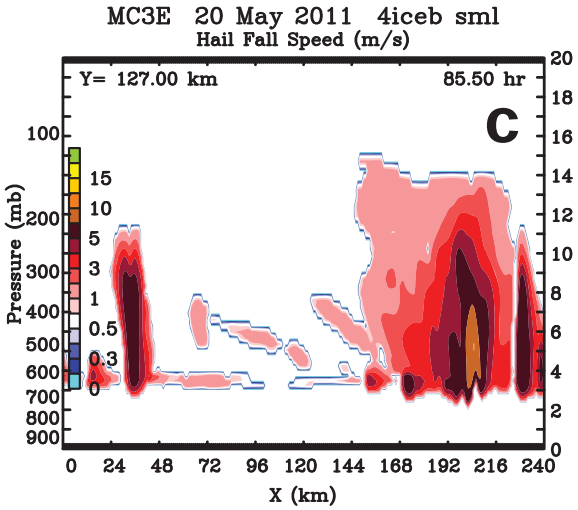
MC3E 20 May 2011 4iceb sml
Hail Fall Speed (m/s)
Y= 127.00 km
85.50 hr
c
Pressure (mb)
X (km)

1591
1592 Figure 4. Same as Fig. 2c except showing vertical cross sections of simulated (a) vertical
1593 velocities (b) graupel fall speeds, and (c) hail fall speeds.
1594

1595
1596
1597
1598

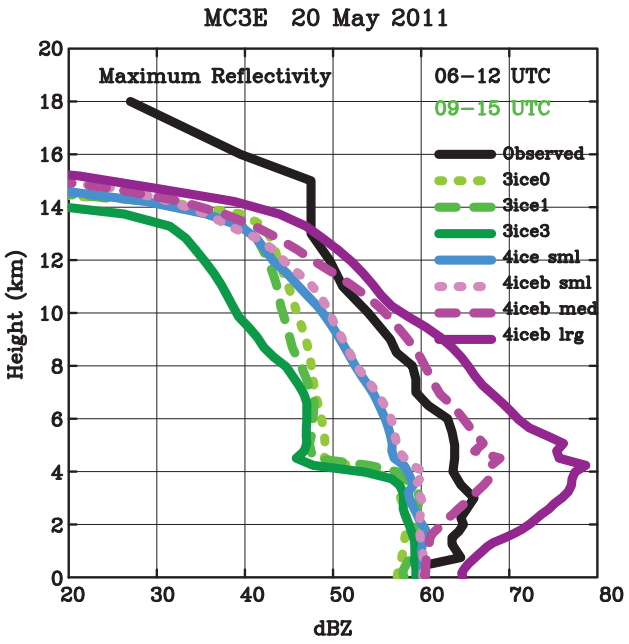

1599 Figure 5. Vertical profiles of maximum radar reflectivity for the 20 May 2011 MC3E case
1600 extracted between 06 and 12 UTC from Doppler radar observations and between 09 and 15 UTC
1601 from the three Goddard 3ICE simulations and four Goddard 4ICE simulations shown in Figure 2.
1602

1603
1604
1605
1606
1607
1608

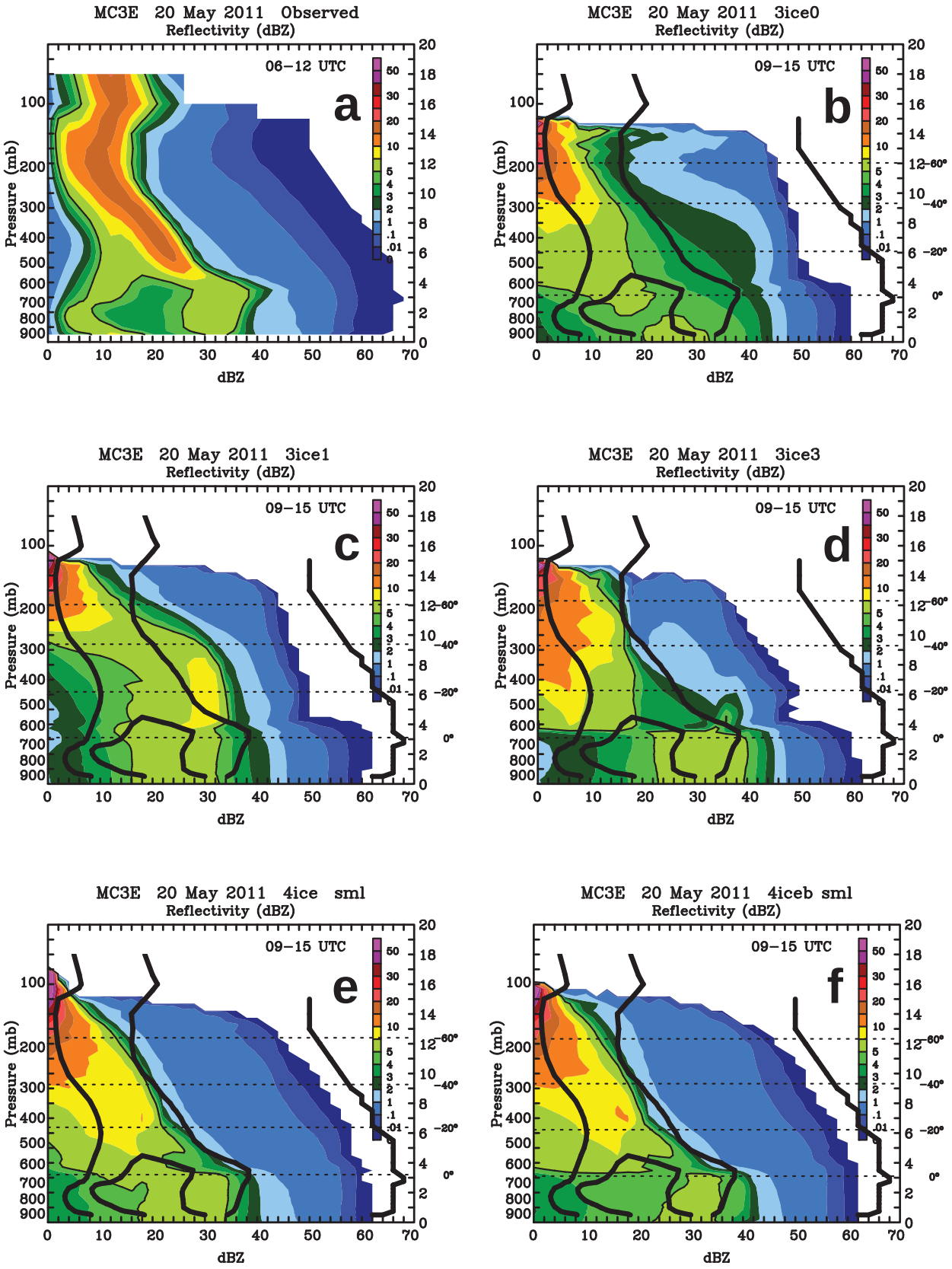

1609

1610

1611

1612

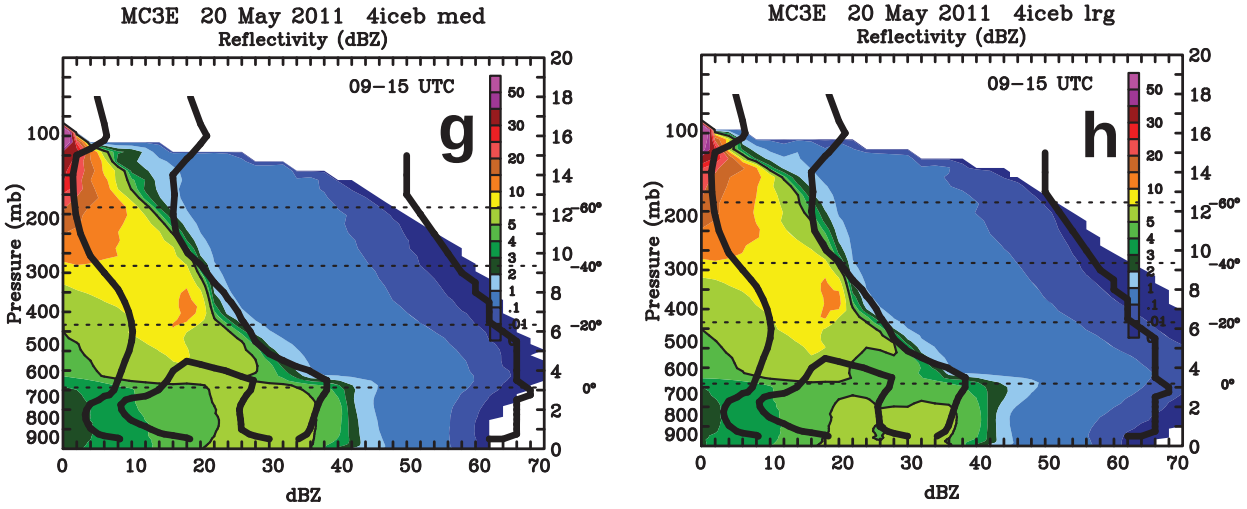

Figure 6. Radar reflectivity CFADs for the 20 May 2011 MC3E case constructed from (a) NEXRAD Doppler radar observations and simulations using the (b) original 3ICE, (c) level 1 improved 3ICE, (d) level 3 improved 3ICE, (e) new 4ICE with smaller hail, (f) new 4ICE with smaller hail and bin rain evaporation correction, (g) new 4ICE with moderate hail and bin rain evaporation correction, and (h) new 4ICE with larger hail and bin rain evaporation correction Goddard microphysics scheme. Heavy thick lines in (b) - (h) show the edges of the core observed frequency probabilities [i.e., the 5 % contours shown in (a)] and the outer limits of the observed frequency distributions [i.e., the 0 % contours shown in (a)]. Right axes are heights in km, while horizontal dashed lines show the level of indicated environmental temperatures in degrees C.

1623
1624

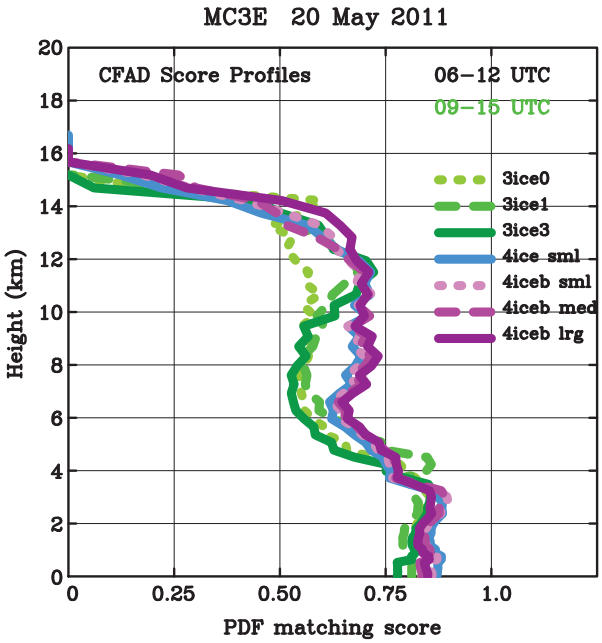
MC3E 20 May 2011
CFAD Score Profiles
06–12 UTC
09–15 UTC
3ice0
3ice1
3ice3
4ice sml
4iceb sml
4iceb med
4iceb lrg
Height (km)
PDF matching score
0
2
4
6
8
10
12
14
16
18
20
0
0.25
0.50
0.75
1.0

Figure 7. Vertical profiles of PDF matching scores (i.e., the amount of overlap between the simulated and observed PDF at each level) for the 20 May 2011 MC3E simulations using the (b) original 3ICE, (c) level 1 improved 3ICE, (d) level 3 improved 3ICE, (e) new 4ICE with smaller hail, (f) new 4ICE with smaller hail and bin rain evaporation correction, (g) new 4ICE with moderate hail and bin rain evaporation correction, and (h) new 4ICE with larger hail and bin rain evaporation correction Goddard microphysics scheme.

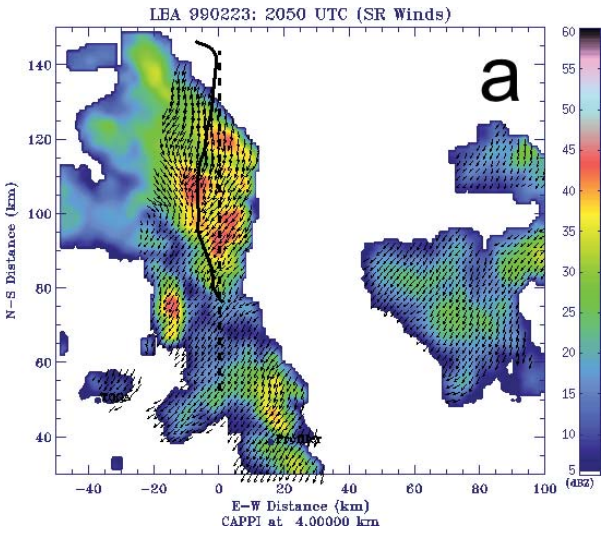

1632
1633

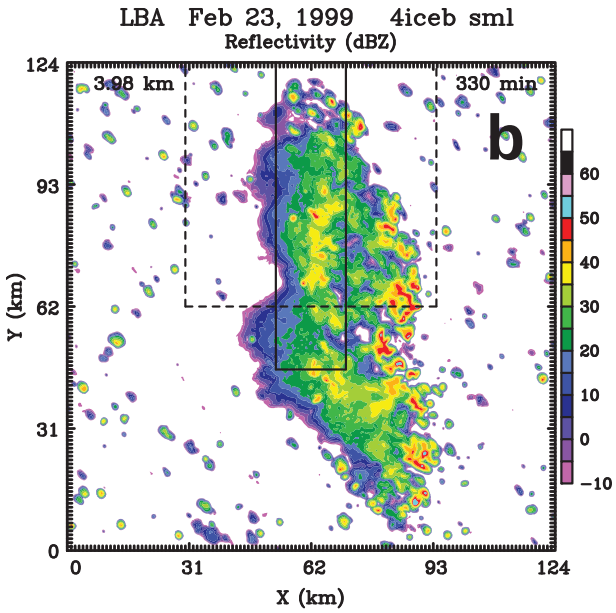

1634

1635

1636

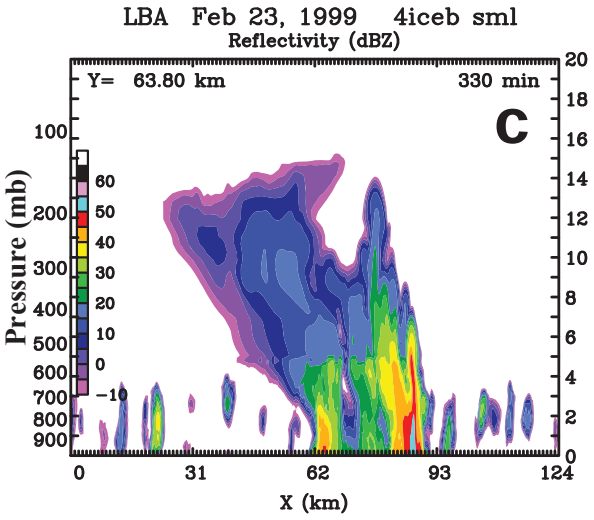

Figure 8. Horizontal cross sections of radar reflectivity for the 23 February 1999 LBA case (a) observed by the S-Pol radar at 20:50 UTC over Amazonia overlaid with storm-relative winds from a dual-Doppler wind analysis and the track of the University of North Dakota Citation aircraft (figure adapted from http://radarmet.atmos.colostate.edu/lba_trmm/23feblba_cappi.html and Lang et al. 2007) and (b) simulated using the new 4ICE scheme with smaller hail and bin rain evaporation correction (4iceb sml) at a simulation time of 330 minutes (21:00 UTC). The vertical east-west cross section of radar reflectivity shown in (c) was taken through the center of the domain from the same simulation and time as (b). The solid rectangle and dashed box shown in (b) denote the north-south oriented rectangular patch of higher sensible/lower latent heat fluxes (Ji Parana) imposed to initiate convection and the analysis domain, respectively.

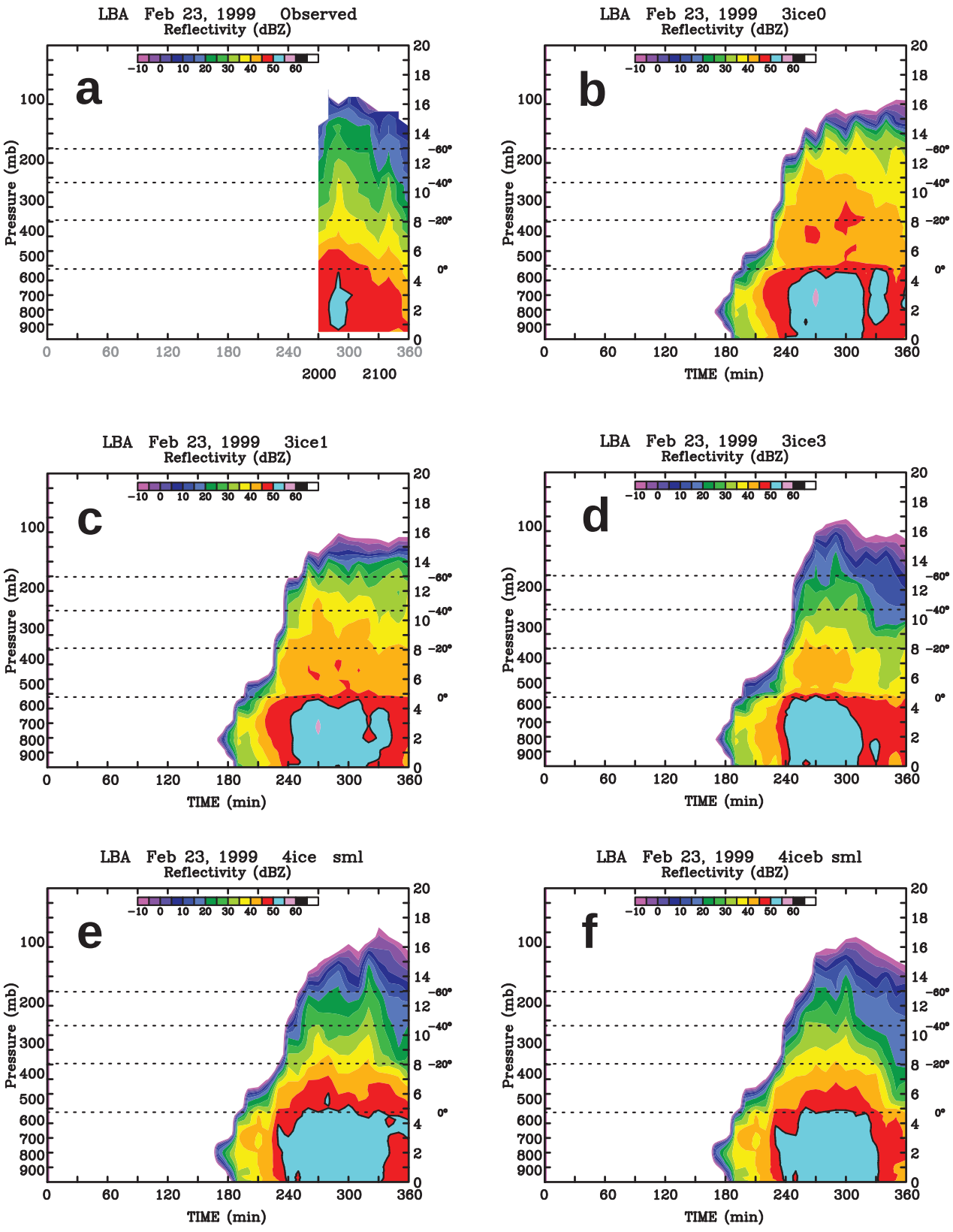
LBA Feb 23, 1999 Observed
Reflectivity (dBZ)
a
LBA Feb 23, 1999 3ice0
Reflectivity (dBZ)
b
LBA Feb 23, 1999 3ice1
Reflectivity (dBZ)
c
LBA Feb 23, 1999 3ice3
Reflectivity (dBZ)
d
LBA Feb 23, 1999 4ice sml
Reflectivity (dBZ)
e
LBA Feb 23, 1999 4iceb sml
Reflectivity (dBZ)
f
−10 0 10 20 30 40 50 60
Pressure (mb)
100 200 300 400 500 600 700 800 900
0 60 120 180 240 300 360
2000 2100
TIME (min)
−60° −40° −20° 0°
0 2 4 6 8 10 12 14 16 18 20

1656
1657

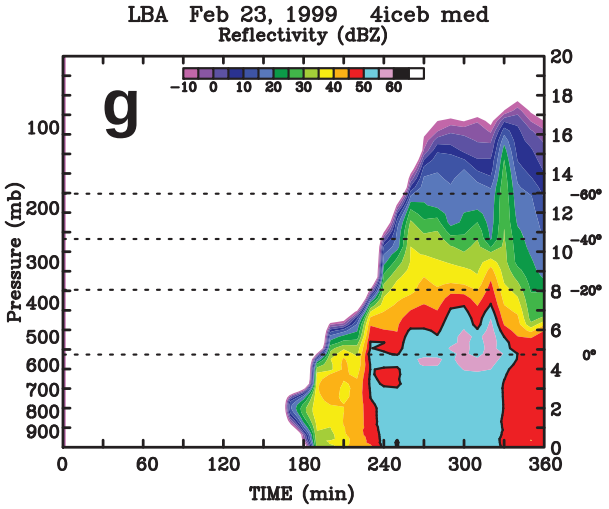
LBA Feb 23, 1999 4iceb med
Reflectivity (dBZ)
g
−10 0 10 20 30 40 50 60
Pressure (mb)
TIME (min)
−60°
−40°
−20°
0°

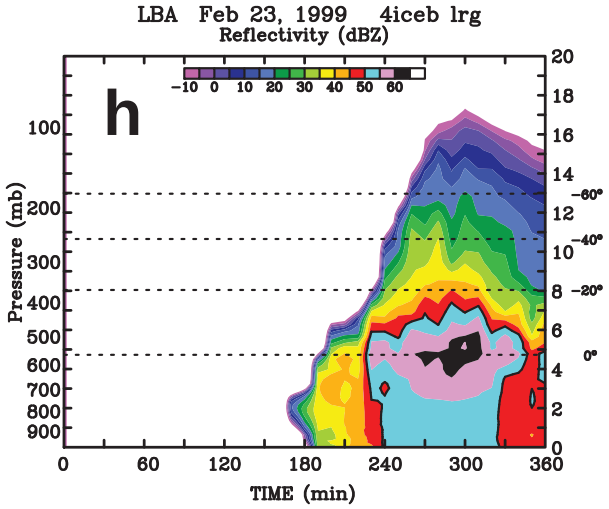
LBA Feb 23, 1999 4iceb lrg
Reflectivity (dBZ)
h
−10 0 10 20 30 40 50 60
Pressure (mb)
TIME (min)
−60°
−40°
−20°
0°

Figure 9. Time-height cross sections of maximum radar reflectivity for the 23 February 1999 LBA case (a) observed by the S-pol ground-based radar and simulated using the (b) original 3ICE, (c) level 1 improved 3ICE, (d) level 3 improved 3ICE, (e) new 4ICE with smaller hail, (f) new 4ICE with smaller hail and bin rain evaporation correction, (g) new 4ICE with moderate hail and bin rain evaporation correction, and (h) new 4ICE with larger hail and bin rain evaporation correction Goddard microphysics scheme. Right axes are heights in km, while horizontal dashed lines show the level of indicated environmental temperatures in degrees C. Model data were taken from a 64 km x 64 km subdomain. Black and gray labels at the bottom of (a) are the UTC and approximate matching times, respectively.

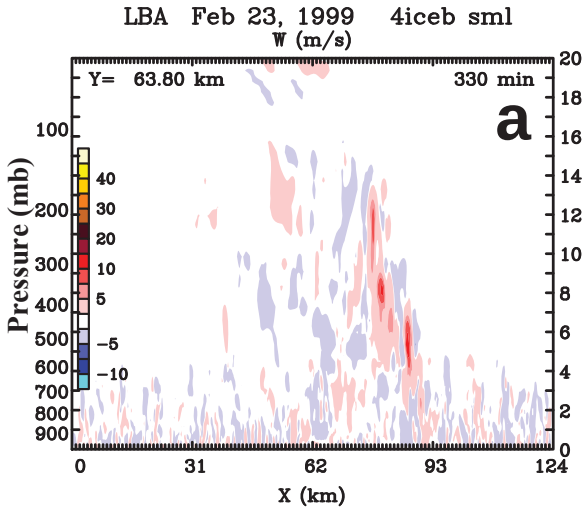
LBA Feb 23, 1999 4iceb sml
W (m/s)
Y= 63.80 km
330 min
a
Pressure (mb)
X (km)
40
30
20
10
5
−5
−10

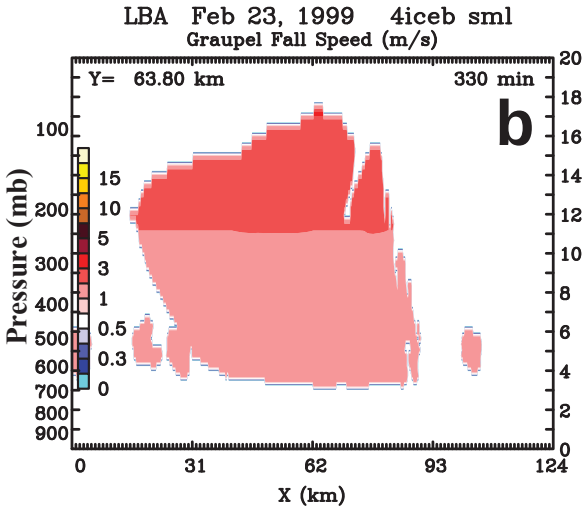
LBA Feb 23, 1999 4iceb sml
Graupel Fall Speed (m/s)
Y= 63.80 km
330 min
b
Pressure (mb)
X (km)
15
10
5
3
1
0.5
0.3
0

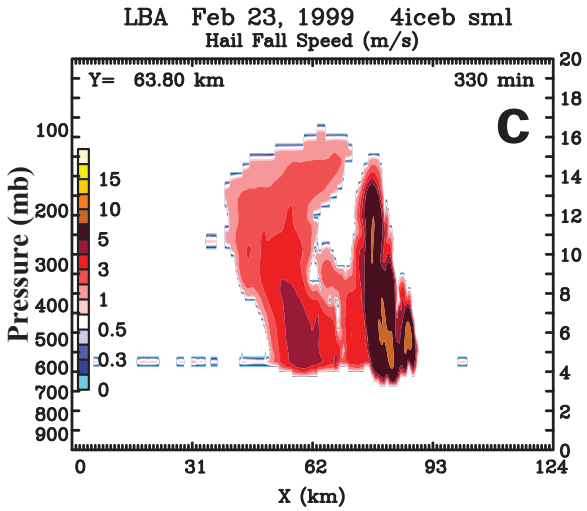
LBA Feb 23, 1999 4iceb sml
Hail Fall Speed (m/s)
Y= 63.80 km
330 min
c
Pressure (mb)
X (km)
15
10
5
3
1
0.5
0.3
0

1674 Figure 10. Same as Fig. 8c except showing vertical cross sections of simulated (a) vertical
1675 velocities (b) graupel fall speeds, and (c) hail fall speeds.
1676
1677

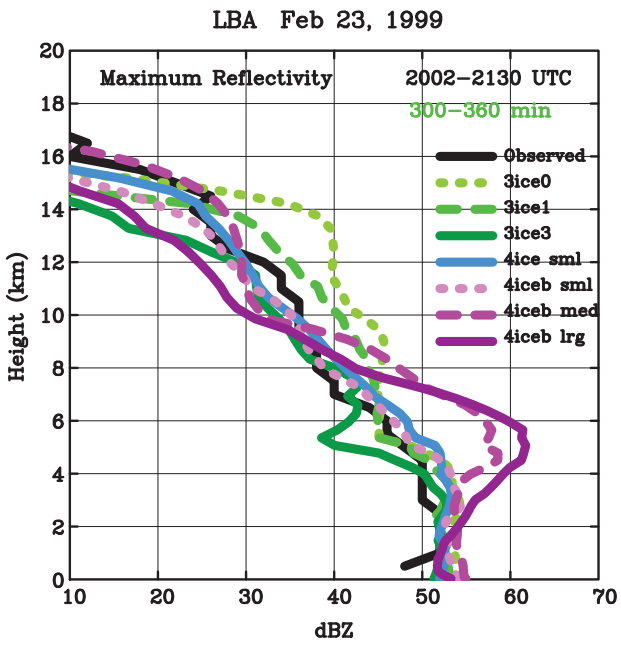
LBA Feb 23, 1999
Maximum Reflectivity
2002–2130 UTC
300–360 min
Observed
3ice0
3ice1
3ice3
4ice sml
4iceb sml
4iceb med
4iceb lrg
Height (km)
dBZ
0
2
4
6
8
10
12
14
16
18
20
10
20
30
40
50
60
70

Figure 11. Vertical profiles of the maximum radar reflectivity for the 23 February 1999 LBA case extracted from the S-pol radar observations and the last 60 minutes of the three Goddard 3ICE simulations and four Goddard 4ICE simulations shown in Figure 6. Model data were taken from a 64 km x 64 km subdomain.

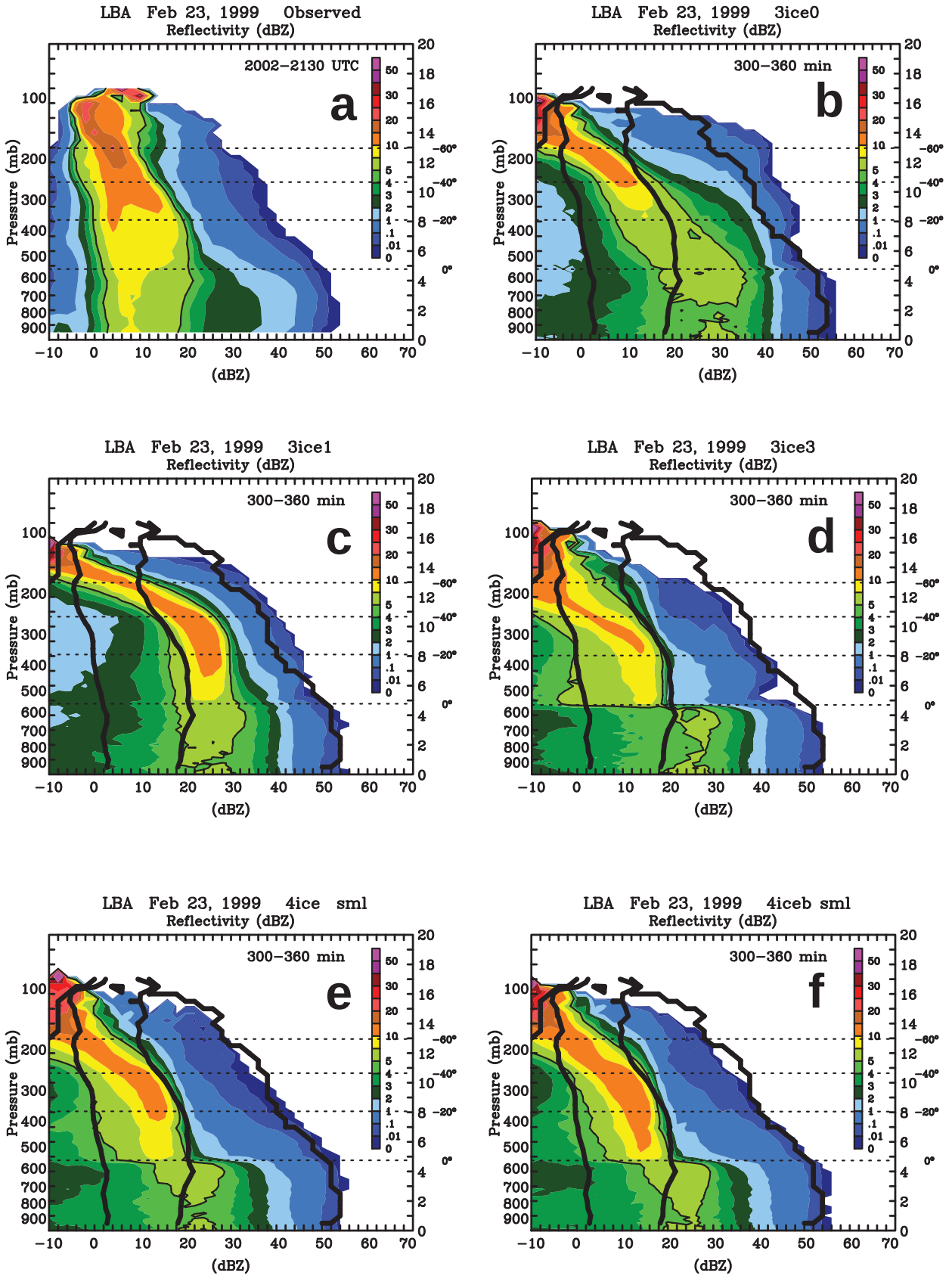
LBA Feb 23, 1999 Observed
Reflectivity (dBZ)
2002–2130 UTC
a
LBA Feb 23, 1999 3ice0
Reflectivity (dBZ)
300–360 min
b
LBA Feb 23, 1999 3ice1
Reflectivity (dBZ)
300–360 min
c
LBA Feb 23, 1999 3ice3
Reflectivity (dBZ)
300–360 min
d
LBA Feb 23, 1999 4ice sml
Reflectivity (dBZ)
300–360 min
e
LBA Feb 23, 1999 4iceb sml
Reflectivity (dBZ)
300–360 min
f
Pressure (mb)
(dBZ)

1732
1733

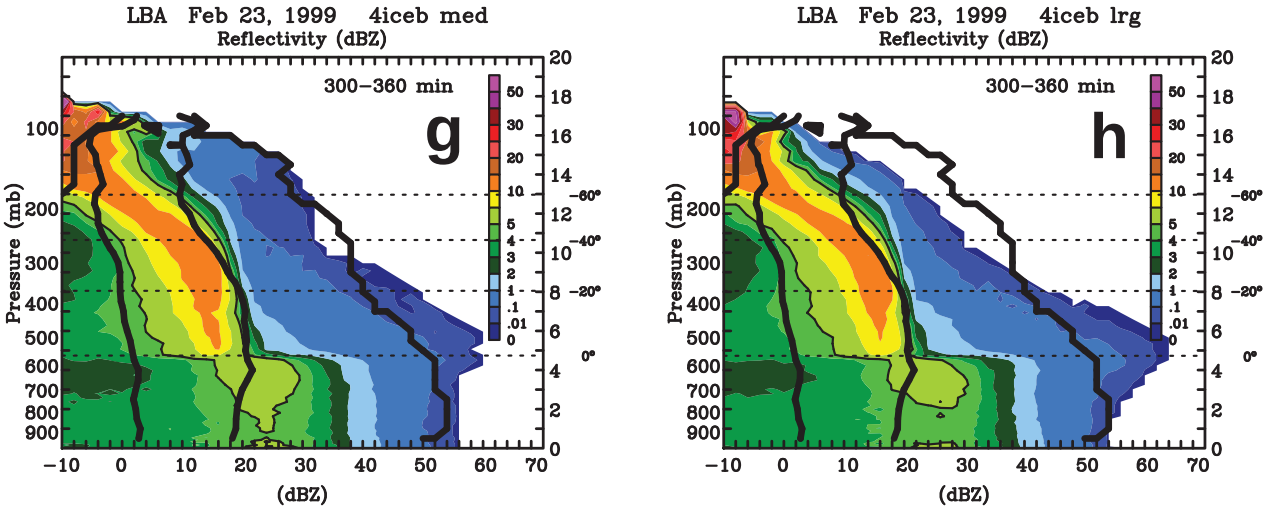
LBA Feb 23, 1999 4iceb med
Reflectivity (dBZ)
300–360 min
g
Pressure (mb)
(dBZ)
LBA Feb 23, 1999 4iceb lrg
Reflectivity (dBZ)
300–360 min
h
Pressure (mb)
(dBZ)

Figure 12. Radar reflectivity CFADs for the 23 February 1999 LBA case constructed from (a) S-pol radar observations and the final 60 minutes of the simulations using the (b) original 3ICE, (c) level 1 improved 3ICE, (d) level 3 improved 3ICE, (e) new 4ICE with smaller hail, (f) new 4ICE with smaller hail and bin rain evaporation correction, (g) new 4ICE with moderate hail and bin rain evaporation correction, and (h) new 4ICE with larger hail and bin rain evaporation correction Goddard microphysics scheme. Heavy thick lines in (b) - (h) show the edges of the core observed frequency probabilities [i.e., the 5 % contours shown in (a)] and the outer limits of the observed frequency distributions [i.e., the 0 % contours shown in (a)]. Right axes are heights in km, while horizontal dashed lines show the level of indicated environmental temperatures in degrees C. Model data were taken from a 64 km x 64 km subdomain.

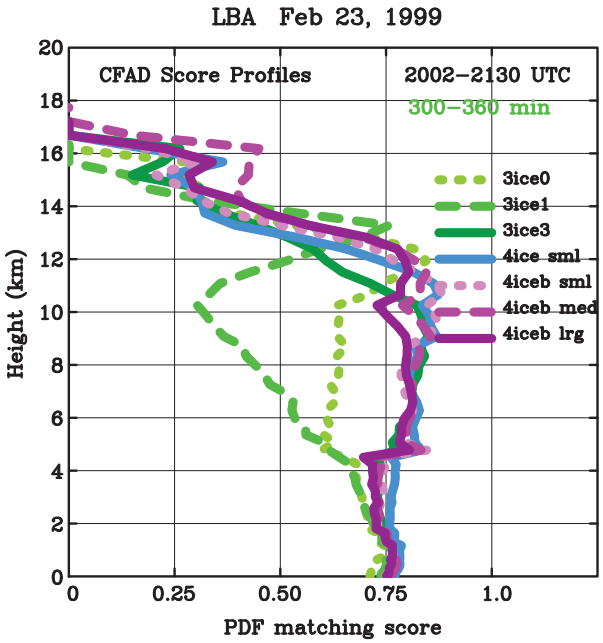
LBA Feb 23, 1999
CFAD Score Profiles
2002–2130 UTC
300–360 min
3ice0
3ice1
3ice3
4ice sml
4iceb sml
4iceb med
4iceb lrg
Height (km)
PDF matching score
0
2
4
6
8
10
12
14
16
18
20
0.25
0.50
0.75
1.0

1747 Figure 13. Vertical profiles of PDF matching scores for the 23 February 1999 LBA simulations
1748 over the final 60 minutes using the (b) original 3ICE, (c) level 1 improved 3ICE, (d) level 3
1749 improved 3ICE, (e) new 4ICE with smaller hail, (f) new 4ICE with smaller hail and bin rain
1750 evaporation correction, (g) new 4ICE with moderate hail and bin rain evaporation correction, and
1751 (h) new 4ICE with larger hail and bin rain evaporation correction Goddard microphysics scheme.
1752 Model data were taken from a 64 km x 64 km subdomain.
1753

1754
1755

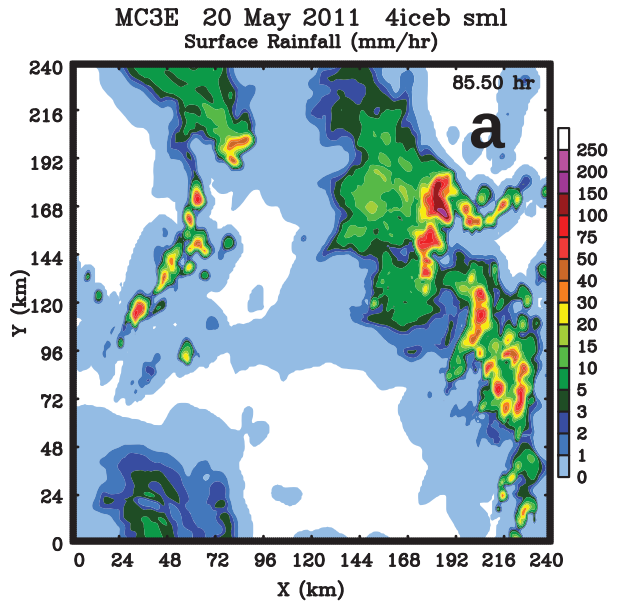
MC3E 20 May 2011 4iceb sml
Surface Rainfall (mm/hr)
85.50 hr
a
Y (km)
X (km)
0 24 48 72 96 120 144 168 192 216 240
250 200 150 100 75 50 40 30 20 15 10 5 3 2 1 0

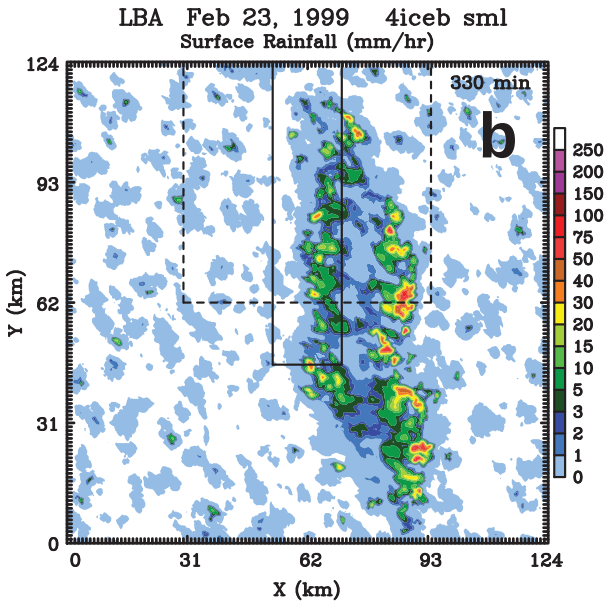
LBA Feb 23, 1999 4iceb sml
Surface Rainfall (mm/hr)
330 min
b
Y (km)
X (km)
0 31 62 93 124
250 200 150 100 75 50 40 30 20 15 10 5 3 2 1 0

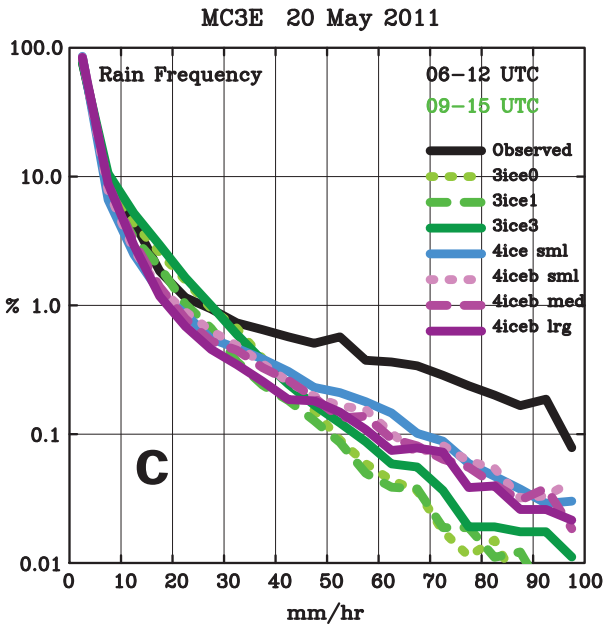
MC3E 20 May 2011
Rain Frequency
06–12 UTC
09–15 UTC
Observed
3ice0
3ice1
3ice3
4ice sml
4iceb sml
4iceb med
4iceb lrg
c
% 1.0
mm/hr
0 10 20 30 40 50 60 70 80 90 100

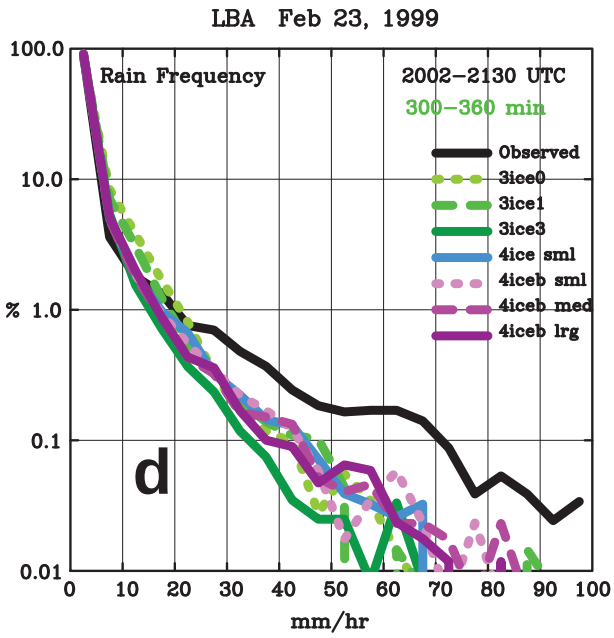
LBA Feb 23, 1999
Rain Frequency
2002–2130 UTC
300–360 min
Observed
3ice0
3ice1
3ice3
4ice sml
4iceb sml
4iceb med
4iceb lrg
d
% 1.0
mm/hr
0 10 20 30 40 50 60 70 80 90 100

1756 Figure 14. Instantaneous surface rainfall rates corresponding to the horizontal radar reflectivity
1757 cross sections shown for the 20 May MC3E case in Fig. 2b (a) and the 23 February LBA case in
1758 Fig. 8b (b). (c) surface rainfall histograms observed by the Doppler radar network around the
1759 MC3E sounding array from 06-12 UTC and simulated with Goddard microphysics from 09-15
1760 UTC for the 20 May MC3E case. (d) surface rainfall histograms derived from ground-based
1761 radar observations collected from 2002-2130 UTC and simulated over the final 60 minutes of
1762 simulation time over a 64 km x 64 km subdomain (shown by the dashed square in panel b) for
1763 the 23 February 1999 case using the Goddard microphysics schemes.

1764

1765
1766

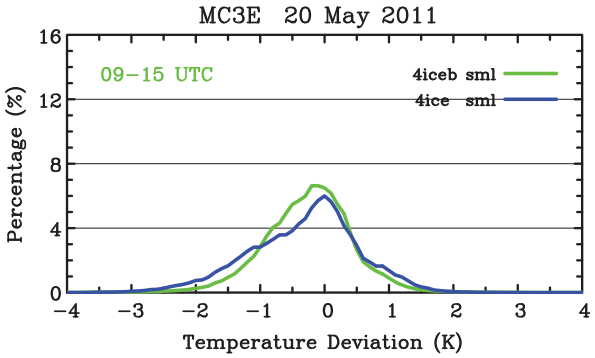
MC3E 20 May 2011
09–15 UTC
4iceb sml
4ice sml
Percentage (%)
Temperature Deviation (K)
16
12
8
4
0
−4
−3
−2
−1
0
1
2
3
4

1767 Figure 15. Distribution of surface cold pool intensities for the 20 May MC3E case for the
1768 smaller hail runs with and without the bin rain evaporation correction, 4iceb sml and 4ice sml,
1769 respectively. Intensities are shown in terms of the surface potential temperature deviations (K)
1770 over the 09 to 15 UTC analysis period for regions where the lowest level rain mixing ratio
1771 exceeds 0.1 g m^{-3}.